Investigation of MoO_3 as an electron injection contact and as a charge transport material in transparent organic light emitting devices

by

Baolin Tian

A thesis
presented to the University of Waterloo
in fulfillment of the
thesis requirement for the degree of
Master of Applied Science
in
Electrical and Computer Engineering

Waterloo, Ontario, Canada, 2011

AUTHOR'S DECLARATION

I hereby declare that I am the sole author of this thesis. This is a true copy of the thesis, including any required final revisions, as accepted by my examiners.

I understand that my thesis may be made electronically available to the public.

Abstract

MoO_3 is investigated for its utilization as a transparent cathode and as a charge transport material in transparent organic light emitting devices. As a transparent cathode, MoO_3 is utilized in combination with a thin metal layer (e.g. Ag) in the form of MoO_3/Ag/MoO_3 (MAM) stack to enable thermal evaporable transparent cathodes. Results show that it is possible to achieve efficient electron injection from the MAM electrode into organic layers by means of incorporating a suitable Electron Injection Layer (EIL) at the interface. Results also show that a MAM electrode can exhibit high optical transmittance, amounting to about 65-80% in the 400-700nm, and a low sheet resistance (9Ω/□). A transparent OLED with a MAM cathode incorporated with a 10nm Bphen: Cs_2CO_3 (10%) EIL is studied. By fine tuning the MAM structure, optimal OLED performance has been achieved: a total luminance of 1300 cd/m^2 (representing ~1000cd/m^2 and ~300cd/m^2 from the bottom and the top, respectively) at 20mA/cm^2 and a corresponding driving voltage of 7.2V. The OLED exhibits a peak transmittance of ~ 90% in the 450-475 nm range, and a transmittance above 45% over the entire visible (i.e. 400-700 nm) range.

As a charge transport, MoO_3 is utilized in combination of various organic hole and electron transport materials in the form of mixtures. Results show that a significantly enhanced bulk conductivity of thin films of MoO_3 and hole-transport organic material mixture is achieved by varying the MoO_3 composition. The mixture films are fabricated in a lateral structure rather than the conventional vertical structure. Experimental results show that the conductivity of NPB: MoO_3 (x) mixture films increases with the MoO_3 composition before its maximum value is reached at x = 50%, which is six orders of magnitude higher than that of the intrinsic MoO_3 film. With further increasing MoO_3 composition, the conductivity of the mixture films decreases and approaches the value of the intrinsic MoO_3. The observed improvement of the film conductivity is attributed to changed bulk and interface properties, whereas the improvement of the bulk material conductivity is the dominant factor. Similar phenomena are also observed in MoO_3 thin films mixed with other hole transport materials (such as TcTa), however not in the thin film mixtures of electron transport materials (e.g., Alq_3 and Bphen) and MoO_3. The I-V results of the hole-only device and electron-only device show that NPB: MoO_3 (50%) mixture has both enhanced electron and hole transport.

Acknowledgements

First and foremost, I would like to thank my supervisors Prof. Hany. Aziz and Prof. Dayan Ban for their constant encouragement, patience, and kindness. It is hard to overstate my gratitude to both of them. With their inspiration, and great efforts to explain things clearly and simply, I enjoy my study and research a lot in the last two years.

I would also like to thank Prof. Bo.Cui and Prof. William.Wong for spending time on reviewing my thesis and attending my MASc. Seminar.

I would like to thank Dandan Song, Qi Wang and Umar Shafique for training me using the equipment in the G2N lab. I sincerely thank them for their valuable discussions, suggestions and constant help in the lab. Also I would like thank Graeme Williams for his help on the AFM measurements and his contribution to my first manuscript.

I sincerely thank Richard Barber, the manager of the Giga to Nano Facility Manager, who is always providing his help in the G2N lab, and pointing out my careless violations of the safety requirement which may be dangerous to me.

A wholehearted thank you goes to the community of students and staff at the University of Waterloo, who have helped with my work through useful discussions, assistance, and maintaining. In particular I would like to thank our group members: Yichun Luo, Radhika Phatak, Hossein Zamani Siboni, Bin Sun, Kewei Wang, Uyxing Vogsaysy, Mina Magdy Aziz Abdelmlek, and Richa Sharma.

Table of Contents

List of Figures

List of Tables

Chapter 1

Introduction

Since the first transistor was invented in AT&T Bell Lab in 1947, inorganic semiconductor Si and Ge have dominated the electronic devices ever since. As a result, the solid state devices took over the vacuum tube based devices and initiated the second electronics revolution. At the end of 20th century, the development of the organic semiconductor is now seen as the third electronics revolution. Organic semiconductors are materials based on organic π-conjugated chains which offer semiconducting properties that can be utilized in electronic devices (Figure 1.1), such as organic field-effect transistors (OFETs) [1- 6], organic light-emitting diodes (OLEDs) [7- 10], and organic solar cells (OSC) [11- 16], and further functions have been demonstrated, such as sensors [17- 19], memory cells [20- 22], or light-emitting transistors [23,24].

Figure 1.1: Various organic semiconductor applications

The most intriguing benefits of using organic materials include mechanical flexibility, high transparency and light weight, which promote new applications such as large area, flexible light sources and displays, transparent light emitting devices and solar cells, low-cost printed integrated circuits or plastic solar cells. Especially, transparent OLEDs and OSCs have become

increasingly interesting in recent years because of their technological potential to high-resolution, high-contrast and high aspect ratio active-matrix displays, and electricity-generating windows, respectively.

This thesis will focus on the investigation of MoO_3 as an electron injection contact and as a charge transport material in transparent OLEDs. In this chapter, the history, the structure, the operation mechanism, materials of OLEDs, transparent OLEDs, as well as the objectives and approaches of this project will be introduced.

OLEDs are light emitting diodes in which the emissive electroluminescent layers are thin films of organic compounds. Electroluminescent (EL) is an optical and electrical phenomenon in which materials emit light in response to the passage of an electric current or to a strong electric field. This is distinct from black body light emission resulting from heat, photoluminescence resulting from absorbing photons, chemical reaction, or other mechanical action [25].

1.1 History and Background

The discovery of organic EL phenomena dates back to early 1950s. A. Bernanose [26] and co-workers at the Nancy University in France applied high voltage alternating current fields in air to acridine orange and quinacrine, and observed EL phenomena in an organic material for the first time. In 1963, Pope's group [27] at New York University first observed EL in pure single crystal of anthracene. However, the anthracene crystal is 20μm thick and the driving voltage is up to 400V, which did not attract many researchers' interest. In 1965, W. Helfrich and W.G. Schneider [28] of the National Research Council in Canada produced double injection recombination EL in an anthracene single crystal for the very first time, which was the forerunner of today's double injection devices. Due to the poor electrical conductivity of contemporary organic materials and the lack of the thin film deposition technology, all the single EL layers were thicker than 1μm and thus required a very high voltage at that time. This was overcome by the discovery and development of highly conductive polymers. In 1977, Alan J. Heeger, Alan G. MacDiarmid and Hideki Shirakawa [29] reported highly conductive oxidized iodine-doped polyacetylene for which they were awarded the Nobel Prize for Chemistry in 2000. In 1982, Vincett and co-workers [30] fabricated 0.6μm anthracene film which reduced the working voltage to 30V. However, the device's quantum efficiency was very low, less than 1%. Therefore, despite the invention of vacuum thermal evaporation of organic material, the EL of organic materials still did not draw considerable attention.

Until 1987, the first thin film OLEDs was reported by Tang and VanSlyke [7] from Eastman Kodak. They used a novel two-layer structure which consisted of the hole transporting and the electron transporting layers. The devices were bright green devices based on tris(8-hydroxyquinoline) aluminum (Alq_3), in which the electron-hole pair recombination and light emission occurred. These devices yielded an external quantum efficiency η_{ext} of 1%. It showed a reduction of operation voltage and an improvement of efficiency, which initiated and led the current research and development of OLEDs. Later, the work on Alq3 and other small π-conjugated molecules demonstrated the potential of small molecular OLEDs. In 1990, Friend and co-workers [8] at the Cavendish Laboratory in Cambridge described the first polymer OLED (PLED) which was a high efficiency green light-emitting polymer based device. They used 100nm poly(p-phenylene vinylene) (PPV) which was fabricated by spin-coating. These two seminal reports opened the door for advanced research in organic EL electronics. In 1992, Heeger and co-workers [31,32] first demonstrated the flexible OLED display using a plastic substrate, which revealed the most charming side of the OLED application before us. In 1997, Forrest et al [33] discovered the phosphorescent EL phenomena. Phosphorescent dyes can convert both singlet and triplet excitons into light, making the devices potentially much more efficient, which broke through the limit that quantum efficiency of organic EL material was lower than 25%. Other important improvements in organic small molecules/ polymer EL development were list in Table 1.

Year	Invention	Reference
1963	Pope et al found electroluminescence in anthracene single crystals.	[27]
1977	Developments in conductive π-conjugated polymers.	[29]
1982	Vincett et al decreased the working voltage of organic EL to below 30V.	[30]
1987	Tang and co-workers first demonstrated EL of Alq_3 thin film.	[7]
1990	Friend et al reported the EL phenomena of PPV polymer under low voltage	[8]
1992	Heeger et al invented the PLED on flexible plastic substrate.	[31,32]
1992	Uchida et al demonstrated blue EL diodes using poly(alkylfluorene).	[34]
1992	Grem et al found the blue EL material PPP	[35]
1993	Sokolik et al found blue EL material PPV copolymer	[36]
1994	Burn et al synthesized conductive copolymer with short alternating	[37,38]

	conjugated and non-conjugated blocks	
1994	Yan et al investigated the mechanism of the photochemical degradation of PPV.	[39]
1994	Kido J. invented the first white OLED device	[40]
1995	Dyreklev et al found the organic EL device emitted polarized light.	[41]
1996	Fou et al fabricated OLEDs based on self-assembled multilayers of poly(phenylene vinylene)	[42]
1996	Epstein et al found organic EL material: Poly(p-pyridine)- and poly(p-pyridyl vinylene)-based polymers	[43]
1997	Forrest et al discovered the phosphorescent EL phenomena	[33]
1998	Hebner et al invented ink-jet printing method to fabricate OLEDs	[44]
2003	Fabricated OLEDs by consecutive deposition of polymers	[45]

Table 1: Important improvement in organic small molecules/ polymer EL devices development

Early organic small molecules/polymers and devices had a poor stability, and therefore people lacked of confidence in the OLEDs industry. However, during the last 30 years, the development of OLEDs has been extraordinarily remarkable: from very dim devices with lifetime less than 1min in air to red and green OLEDs and blue OLEDs with a lifetime over 200000hrs and 100000 hrs, respectively, at the brightness of 150 Cd/m^2[46,47].

1.2 OLEDs Structure & Operation Mechanism

The OLED has a typical structure where organic materials are sandwiched between two electrodes: a transparent anode with a high work function and a metal cathode with a low work function, which form low energy barriers at the electrode-organic interfaces for both contacts in order to inject the same amount of holes and electrons. These energy barriers are critical for the injection of charge carriers, and consequently essential to the OLEDs efficiency. With the knowledge of the OLEDs structure and corresponding energy band diagram of each thin film layer, the OLEDs operation mechanism can be concluded into four aspects (Figure 1.2): 1.charge carrier injection, 2.charge carrier transport, 3.electron-hole pair capture and exciton formation, 4. radiative decay of exciton. The carrier injection and carrier transport are the two most fundamental physics mechanism in OLEDs, which have crucial influence on device performance

such as quantum efficiency, power consumption and etc. Details of OLEDs structure and operation mechanism will be discussed respectively in next several sections.

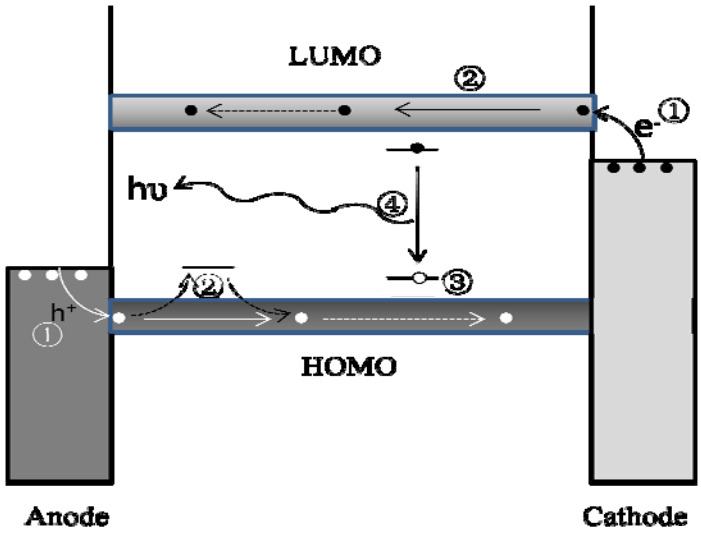

Figure 1.2: Aspects of OLED physics: 1.charge carrier injection, 2.charge carrier transport, 3.electron-hole pair capture and exciton formation, 4.radiative decay of exciton.

1.2.1 Single layer, double layer and multilayer structure

At the beginning of the OLEDs development, a single layer of organic material was sandwiched between two electrodes (Figure 1.3(a)) [27]. However, the single layer devices had very poor efficiency. Since the mobility of electrons and holes are different in organic materials, one type of the carriers (electrons or holes) was accumulated at one metal-organic interface where all the recombination happened in OLEDs. Thus, the surplus electrons or holes will not recombine, which results in low operation efficiency. Until 1987, Tang and VanSlyke [7] demonstrated comparably efficient OLEDs with a double layer structure (see Figure 1.3(b)). The double layer structure contains two organic layers: the hole transport layer (HTL) and the electron transport layer (ETL). This structure allows both of the electrons and holes move easily inside ETL and HTL, respectively. In addition, ETL may block holes from moving towards the cathode, and the same analogy applies to HTL and electrons. Therefore, the holes and electrons will meet in the middle of two organic layers and recombine, which significantly improves the efficiency of OLEDs.

Today, in order to achieve much highly efficient OLEDs, the multilayer structures are employed in the design of OLEDs (Figure 1.3(c)), which contain different functional layers: electron injection layers (EIL), electron transport layers (ETL), emission layers (EL), hole

transport layers (HTL) and hole injection layers (HIL), as well as special carrier blocking layers. When a forward bias is applied to the OLED, holes and electrons are injected from HIL and EIL, transported through HTL and ETL, respectively, and met and captured to form exitons in EML. Finally the exitons either decay radiatively to emit photons or dissipate non-radiatively. The thin EIL and HIL may dramatically decrease the energetic barriers and achieve high efficiency, which we will discuss more in detail later.

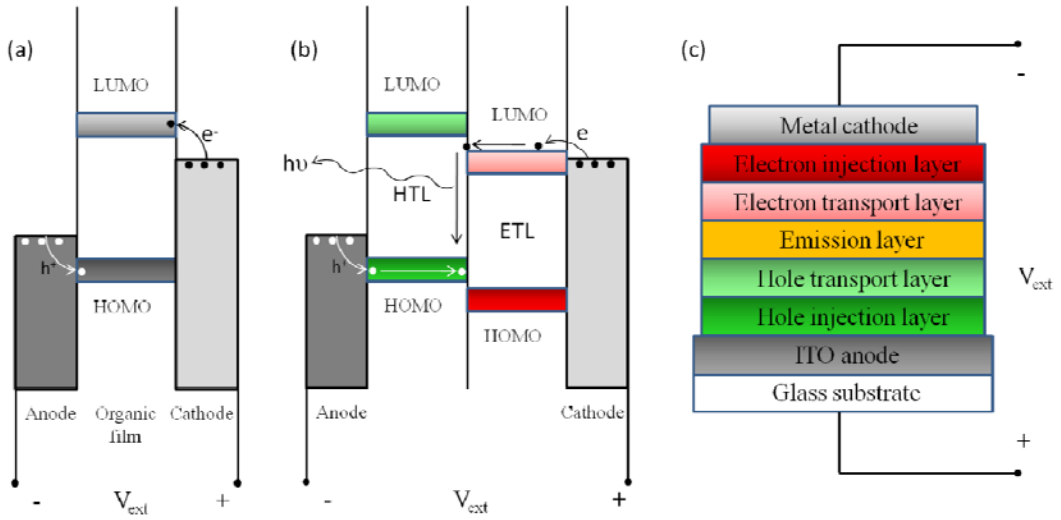

Figure 1.3: Structure of OLEDs: (a) single layer structure, (b) double layer structure and (c) complex multilayer structure.

1.2.2 Charge carrier injection from contacts

At the beginning of the research on the carrier injection at the organic/electrode interface, the energy barriers for the charge injection have been commonly estimated by assuming vacuum-level alignment across the interface. The energy barrier is the difference in energy between the electrode Fermi level (E_f) and the organic transport levels at the interface (HOMO or LUMO). As shown in Figure 1.4, the work function of the metal Φ_m is the distance between Fermi level E_f and vacuum level. The ionization energy (IE) and the electron affinity (EA) of the organic material are the distances between vacuum level and HOMO and LUMO, respectively. As the organic LUMO level is typically higher than the metal E_f level, electrons at metal E_f level are facing a potential barrier $\Phi_b = \Phi_m - EA$.

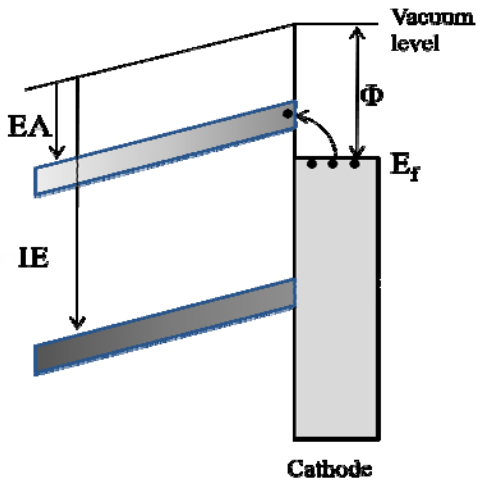

Figure 1.4: Sketch of the OLED under forward bias.

Without external voltage, the electrons cannot be injected into the unoccupied orbital of the organic material. When a forward bias is applied to the device, the LUMO level of the organic material slants and forms a triangular potential barrier at the interface. Based on the tunneling model Parker [48] proposed in 1994, the electrons distributed near E_f level have certain probability to tunnel through the triangular potential barrier and be injected into the organic LUMO level. Parker investigated different thicknesses of the organic material (MEH-PPV) with different cathode materials, and it turned that the current density-electrical field (J-E) characteristics fitted very well with the calculated results from the Fowler-Nordheim equation based on the triangular potential barrier (Figure 1.5). The injection of holes is more or less the same as that of electrons, while the holes face an energy barrier Φ_b=IE-Φ_m when they are injected from anode into the organic HOMO level.

$$j_{FN} = \frac{A^*}{\Phi_B}\left(\frac{qF}{\alpha k_B}\right)^2 \exp\left(-\frac{2\alpha\Phi_B^{3/2}}{3qF}\right)$$

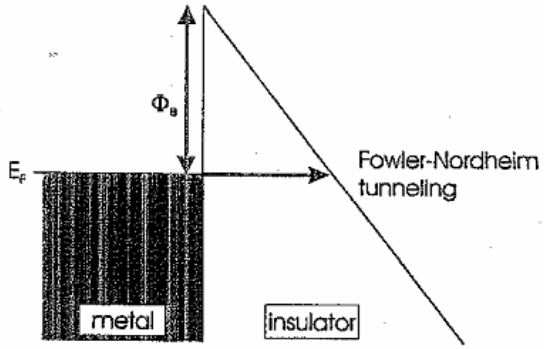

Figure 1.5: Quantum mechanical tunneling of electrons through a triangular energy barrier.

While Parker's quantum tunneling model has been well accepted, the triangular energy barrier model is over simplified and does not fit well with some experiment results. One important problem which was not considered in Parker's model is the influence of the image force. When electrons leave the metal and are injected into the organic material, due to the electrical field of individual electron, the metal surface will have positive induced charges attracting these electrons. This attracting force that electrons experienced is termed as the image force which prevents the escape of the electron from the metal surface. A modified Richardson-Schottky model included the effect of the image force potential is shown in Figure 1.6. After considering image force, the height of the potential barrier is lower and the injection of carrier is enhanced.

$$j_{RS} = A^* T^2 \exp\left(-\frac{\Phi_B - \Delta\Phi}{k_B T}\right), \qquad \Delta\Phi = \sqrt{\frac{q^3 \cdot F}{4\pi \cdot \varepsilon_r \cdot \varepsilon_0}}$$

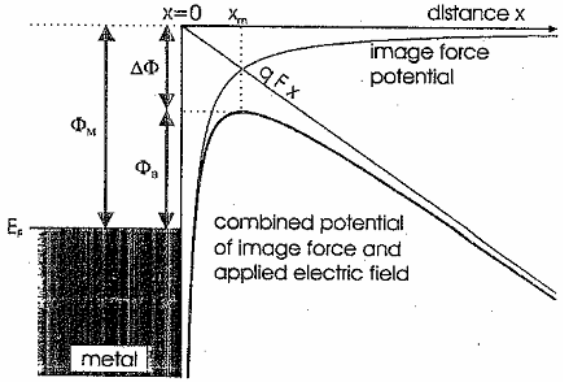

Figure 1.6: Field-assisted thermionic injection over the image force barrier.

In the above discussions, we assume the potential barrier height is $\Phi_b=\Phi_m$-EA, which defaults the vacuum level aligns across the electrode-organic interface. However, this assumption is not accurate in reality. Since the E_f level of metal and organic materials is different, under the equilibrium state, the distribution of the electron density at the metal- organic interface will be modified to achieve E_f level alignment across the whole system. In inorganic semiconductor-metal interface, if the E_f level of metal is lower than that of the inorganic semiconductor, electrons will flow from the semiconductor to the metal and the holes left inside semiconductor will form space charge region. The electrical field due to those space charges will bend the energy levels inside the space charge region, and form a Schottky barrier shown in Figure 1.7.

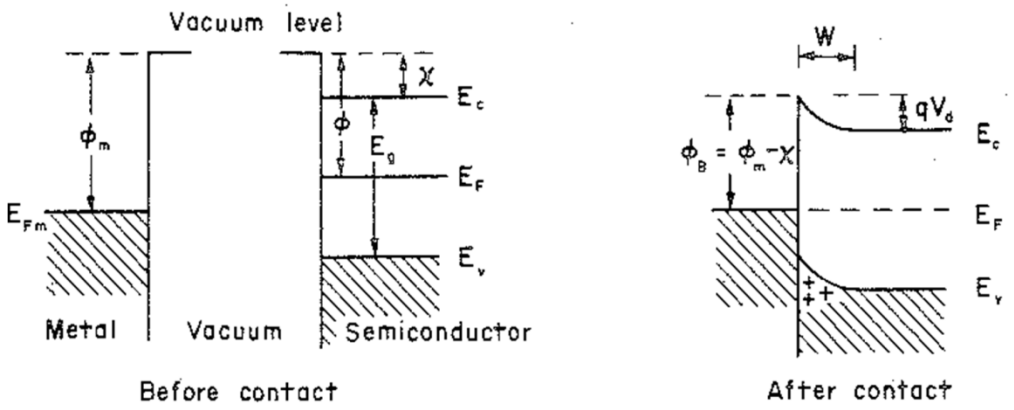

Figure 1.7: Energy band diagrams for the interface between metal and inorganic semiconductor with E_f of metal lower than E_f of semiconductor

However, the band gap of organic semiconductors is typically between 1.5-3eV, which is much larger than the thermal energy at room temperature (26 meV). Therefore, the amount of electrons at LUMO level and the amount of holes at HOMO level can be ignored. In consequence, the interface between metal and organic semiconductor will not form Schottky barrier. Ultraviolet and inverse photoelectron spectroscopy (UPS, IPES) allow the magnitude of the hole and the electron injection barriers to be assessed. Utilizing these methods, researchers observed an interface dipole layer with a thickness of several monolayers was formed at the interface when depositing organic thin film on metal. They contributed this phenomenon to the carrier transfer, redistribution of electron cloud, and chemical reaction at the interface, all of which induced the changes of the electrical potential at the metal surface. This organic-metal interaction is shown in Figure 1.8, which shows a quantitative picture of the interface energy diagram. Before contact, the metal and the organic material have no interactions. The metal work function has two contributions, namely, the bulk chemical potential (μ_{bulk}) and the surface dipole (SD), which is due to the electron spilling out into the vacuum at the free surface. However, as the two materials contact each other, the SD of the metal surface reduces to SD', due to the adsorption of the organic molecules pushing back the electron density of the metal surface that was spilling out into the vacuum. This reduced SD' causes the potential barrier decrease at the interface, and this decrease can be up to 1eV. More research shows that the direction of the interface dipole is the same (point from organic material to metal) for most of the metal- organic contact, which mades the organic material to be positively charged. The direction of the interface dipole will facilitate the electron injection, however, prevent the hole injection.

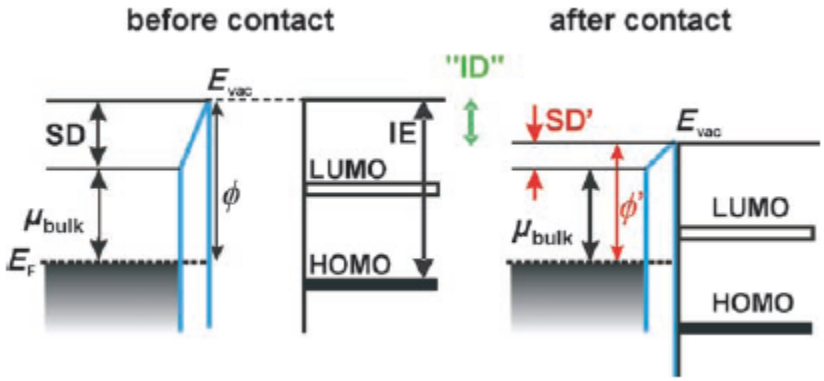

Figure 1.8: Schematic energy levels at an organic-metal interface, before and after contact.

1.2.3 Charge transport

After the injection of carriers into organic semiconductors, the charge carriers start to transport inside organic semiconductors under the external electrical field. In inorganic semiconductor crystal, due to the well ordered structure and strong interaction between the covalent bond among atoms, electrons can freely move inside the crystal. However, organic semiconductor molecules are bonded by the Van de Waals force, and thus the overlap among molecules' electron clouds is very weak. In consequence, electrons are locally free to move inside a molecule, and it is very difficult for electrons to move from one molecule to another. Besides that, organic semiconductor films are typically in amorphous state rather than crystal state because of the relative large molecule size. Therefore, charge carriers in organic semiconductors have a low mobility, normally between 10^{-8} ~10^{-2} $cm^2V^{-1}s^{-1}$.

As mentioned above, the attractive or repulsive force between organic molecules is the Van der Waals force that is very weak. Thus, it leads to a disordered structure of the organic semiconductor in which each molecule is in a different energy environment, and therefore, it results in a Gaussian distribution density of states (Figure 1.9).

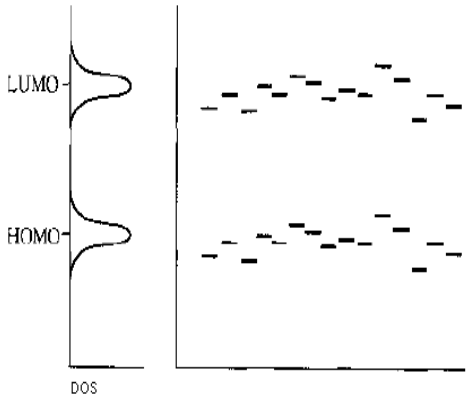

Figure 1.9: Gaussian distribution of states in amorphous solid, the width of the Gaussian density of states in an amorphous solid is typically in the range of σ=80-120 meV.

1.2.3.1 Space Charge Limited Conduction (SCLC)

Organic semiconductors have a very low intrinsic carrier density. Consequently, the conduction mechanism of the organic semiconductors is similar as that of insulators, which relies on the injection of electrons and holes into the LUMO and the HOMO, respectively, from external voltage source. Due to the disordered structure and the chemical or structural defects, organic semiconductors contain many trap states which can capture the injected charge carriers

and form a large amount of space charge inside the semiconductor. As all these space charges prevent the transport of the carriers, it is termed as space charge limited current effect [49].

Considering the ideal case that organic semiconductor has no traps, the carriers transport is similar as the drift transport in inorganic semiconductors under an electrical field. So the electron current can be described as:

$$I = nev$$

Where, n is the electron density; v is the average drift velocity; e is the electron charge. Since $I = Q/t$, Q is the amount of injected charges per unit area, t is the carrier transport time from anode to cathode,

$$Q = neL$$

L is the distance between anode and cathode. Semiconductor acts as a capacitor due to the distribution of space charges:

$$Q = CV$$

C is the capacitor per unit area, and $C = 2\varepsilon/L_{eff}$, where ε is the material dielectric constant, however, the carriers are distributed everywhere from anode to cathode. Therefore, the actual effective distance L_{eff} is smaller than L. If we assume that carriers are evenly distributed in space, then

$$L_{eff} = L/2 \quad \text{and} \quad I = \varepsilon v V/L^2$$

Under a low electrical field, we assume that mobility μ is not influenced by electrical field E,

$$v = \mu E = \mu V/L$$

And

$$I = \varepsilon\mu(V^2/L^3)$$

This is the ideal insulator space charge limited current equation. In real organic semiconductor, the situation is quite different. Due to the large amount of trap states, many trapped carriers are not contributed to the current conduction; therefore the real current value is much smaller than the calculated value based on the above equation. However, the same idea and derivation process are still hold in real situation after considering that the charge carriers not only contribute to the current conduction but also built the internal electrical field which prevents the current transport. After considering the trapped carriers, non-uniformity of electrical field, and all other influenced factors, the current is:

$$I \propto V^{m+1}/L^{2m+1}$$

Where m is a constant related to the trap distribution, typically m is between 6~8. Many experiment results fit very well into this equation. And it can be seen from Figure 1.10: the current- voltage characteristics of OLEDs with different ETL: Alq_3, Gaq_3 and Inq_3 by Burrows and Forrest [50]. At low voltage, m=0 fits the Ohm's law; at high voltage, m is approximately 8 which fits the space charge limited current. As seen in Figure 1.10, the experiment data are well fitted with the space charge limited conduction model.

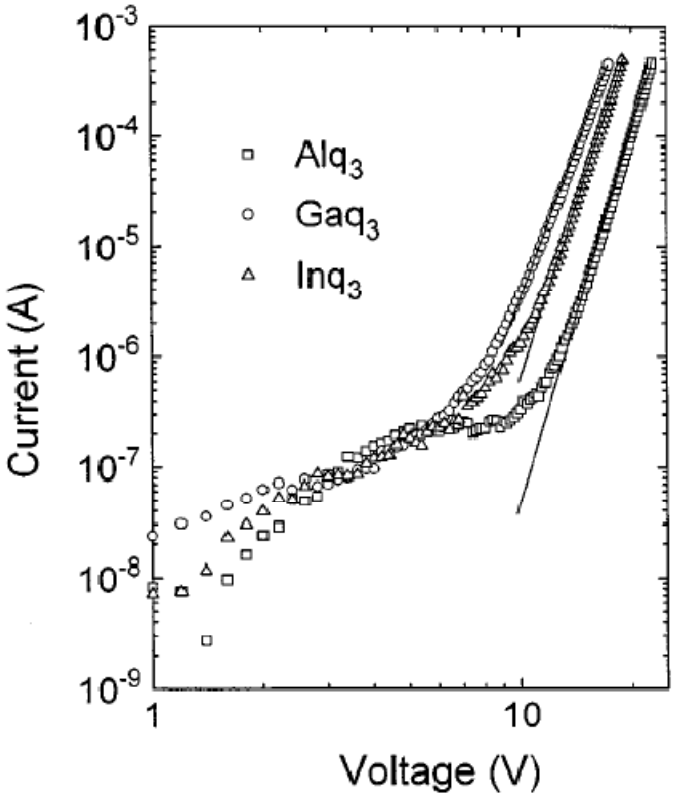

Figure 1.10: Current – voltage characteristics of OLEDs with structure: ITO/TPD (20nm)/ Alq_3, Gaq_3 or Inq_3 (40nm)/ Mg:Ag. Solid lines show fits to the SCLC model with m around 8.

1.2.3.2 Hopping transport

When we derived the current equation of SCLC, we assumed that the carrier mobility μ is not influenced by the electrical field E. However, this is not true in a real situation. Early in 1980s, researchers had already found that the carrier mobility in organic material had a strong dependence on the electrical field and the temperature. And it is described by Poole-Frenkel equation:

$$\mu = \mu_0 \exp\left(-\frac{\theta}{kT}\right) \exp\left(\gamma\sqrt{E}\right)$$

Where μ_0, θ, γ are factors related to material, k is Boltzmann constant, T is the absolute temperature, E is the electrical field.

The reason behind the dependence of the carrier mobility in organic materials on the electrical field and the temperature is the charge carrier hopping transport mechanism. In inorganic semiconductor crystal, atoms are tightly bonded to each other by covalent bonds, and form a unity where atoms' wave functions at high energy state overlap each other and form continuous conduction band (CB) and valence band (VB). Electrons in CB and VB are all free to move in the system (known as band transport), as shown in Figure 1.11(a). For organic semiconductors shown in Figure 1.11(b), all the atoms in each molecule are tightly bonded to one another by covalent bonds, whereas each molecule is unaided and bonds with others through weak Van de Waals force. Therefore, molecule's LUMO and HOMO wave functions only overlap a little bit. When an electron transports from one molecule to another, it has to overcome a potential barrier with a small probability. This is the reason why organic semiconductor has a poor electrical conductivity compare with inorganic semiconductor.

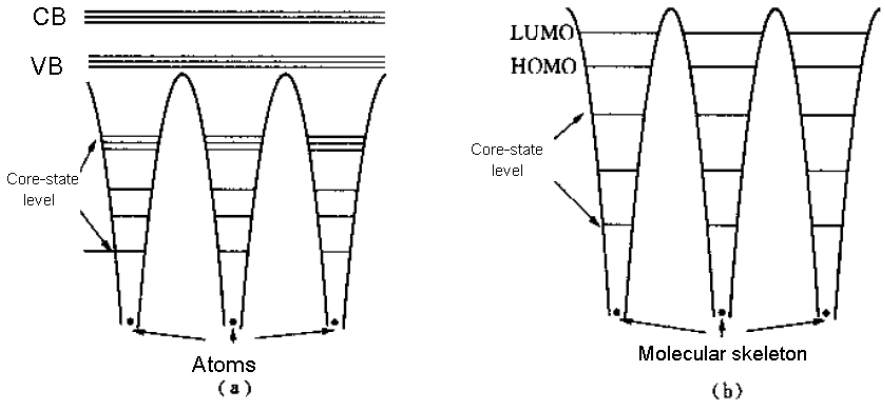

Figure 1.11: Schematic energy bands of (a) inorganic semiconductor, (b) organic semiconductor

Without applied field, the carriers locally vibrate at the HOMO or LUMO level, and they have a certain probability to tunnel through the barriers to the adjacent molecules. Because the carriers have the same probability of tunneling to all the adjacent molecules, there is no overall current inside the material. When we apply a field, molecules in different positions have different potential. In this case, carriers have a higher probability to tunnel from a high potential molecule to a low potential molecule. After the carrier successfully tunnels to a new molecule, there is a

very low probability for the same carrier to tunnel again. Consequently, the carriers will stay in the molecule until next successful tunneling. This carrier transport mechanism in organic semiconductors is commonly referred to as hopping transport.

1.2.4 Electron-hole capture and exciton formation

Since electrons and holes are injected into the organic semiconductor, they are moving towards each other under the influence of electrical field and getting closer to each other under the attraction of Coulomb force. Part of the electrons and holes are captured in one molecule and form excitons. Exciton is an electronic excitation in the solid, essentially a bound pair of electron and hole at a non-ground energy level. And it can be viewed as quasi-particles which are capable of diffusing and migrating.

Depending on the distance and the interaction between the electrons and holes, and the degree of delocalization of the electrons around the the hole, exciton can be classified as: (a) Frenkel excitons, (b) Wannier-Mott excitons and (c) Charge-transfer excitons (Figure 1.12).

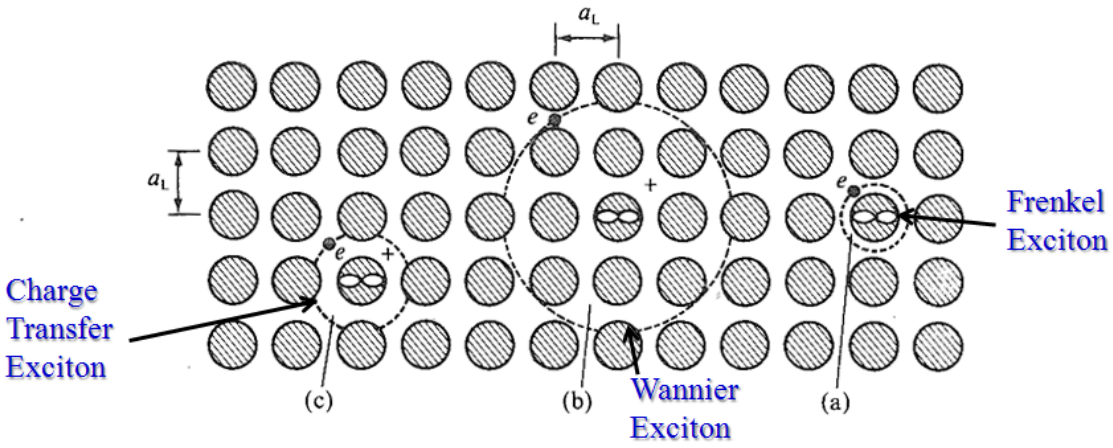

Figure 1.12: (a) The small-radius Frenkel exciton in which the radius a is small in comparison with a lattice constant a_L. (b)The large-radius Wannier-Mott exciton in which the radius a is large in comparison with a lattice constant. (c) The intermediate or charge-transfer exciton, in this case, a nearest neighbor.

Frenkel exciton (Figure 1.12(a)) corresponds to a correlated electron-hole pair localized on a single molecule. The interaction between an electron and a hole may be strong with a typical binding energy on the order of 0.1 to 1eV and thus the excitons tend to be small. Its radius is comparable to the size of the molecule (typically < 5 Å), or smaller than the intermolecular distance. Because the hole and the correlated electron are located on the same molecular site, Frenkel excitons are neutral and the electron and the hole are moving as a whole. They are

typically found in alkalihalide crystal and in organic molecules crystal composed of aromatic molecules, such as anthracene and tetracene.

As the other extreme, Wannier-Mott (WM) excitons (Figure 1.12(b)) occur in crystalline materials with strong intermolecular interactions. Because of a significant potential overlap between neighbouring lattice points in such materials, coulombic interaction between the electron and the hole of the exciton was reduced. This results in a large exciton radius (40-100Å) whose size is as many times as the size of the lattice constant. As the distance between the electron and the hole is relative large in this case, the medium between the electron and the hole can be treated as a continuous homogeneous dielectric medium with dielectric constant ε. Therefore, the attractive force between the electron and the hole is $e^2/\varepsilon r^2$, similar to the attraction force between an unit negative charge and an unit positive charge. Consequently, the WM exciton has an energy level structure which is similar to that of hydrogen atom. Due to the weak interaction between the electron and the hole, the WM excitons are very unstable and easy to dissociate into independent electrons and holes. WM excitons occur in uncorrelated, crystalline materials (as are most conventional inorganic Crystals) rather than molecular organic solids.

Between these two cases, charge-transfer (CT) excitons are of an intermediate size, have a spatial extent of 1-2 lattice constants. The promoted electron is transferred to the nearest or next nearest neighbouring molecule site, but remains correlated to its parent hole. Because the electron and the hole reside on different sites, CT excitons have a dipole moment, and as such sometimes considered as an unrelaxed polaron pair with the positive and negative polarons located on discrete, identifiable, and nearly adjacent molecules. However, this localized picture is true only if each molecule forms a deep potential well in which charges are confined by the self-induced rearrangement of the local environment by the exciton dipole. Such a localized potential would be expected for a molecular crystal with weak intermolecular interactions and small overlap between the neighbouring orbitals.

As we know the electrons are Fermions, an electron has a spin quantum number of 1/2. In the Z direction, the component of spin angular momentum can be ±ħ/2. When the spin angular momentum of two electrons coupled, the spin angular momentum quantum number can be 0 or 1 after coupling. When the quantum number is 0, the Z component of spin angular momentum can be and only can be 0; however, when the quantum number is 1, the Z component of the spin angular momentum can be +ħ/2, 0, -ħ/2, three different states. According to the Pauli Exclusion Principle, each quantum state can simultaneously have up to two electrons with different spins. The total spin angular momentum of the two electrons is 0. Even though one of the two electrons

is excited to an excited state (LUMO), the electron and the one left on ground state (HOMO) still have a total spin angular momentum 0. This excited state with a total spin angular momentum of 0 is called singlet. If the exciton's electron and hole are not from photoluminescence but from the injection from the external source, which is our case for OLEDs, the total spin angular momentum quantum number of the exciton can be 0 and 1 as well. For the case that total spin quantum number is 1, the Z component of the spin angular momentum can be +ħ/2, 0, -ħ/2 three states. Therefore, the excited state with a total spin angular momentum of 1 is called triplet (Figure 1.13). In general, single-triplet ratio of excitons formed by external injected electrons and holes is 1:3.

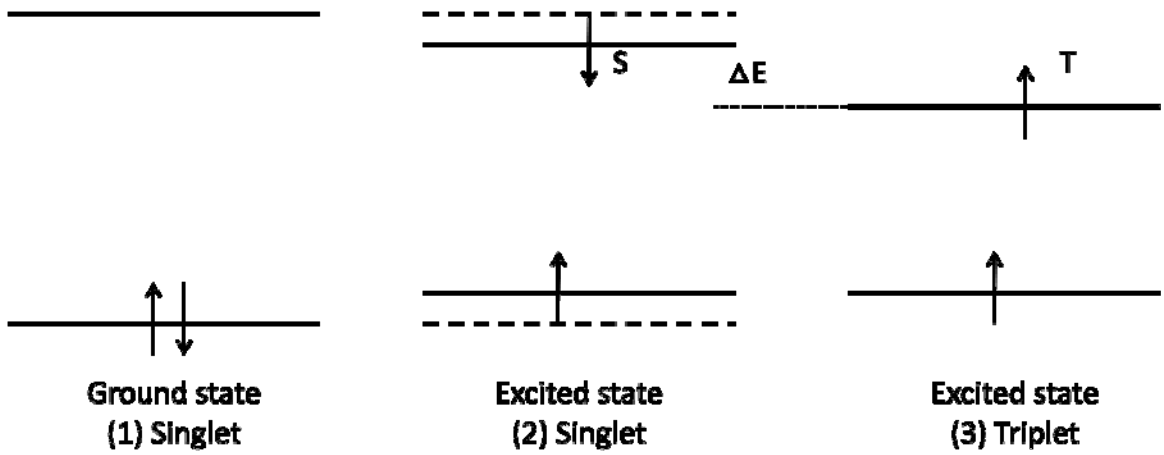

Figure 1.13: Energy state of ground singlet, excited singlet, and excited triplet

The energetic difference between an excited state sitting on one molecule and a pair of uncorrelated negative and positive carriers sitting on different molecules far apart defines the exciton binding energy, typically 0.5 to 1eV. From Figure 1.13 (2), we can clearly see that due to exciton binding energy the optical band gap between ground state and the first excited singlet state is considerably narrower than singlet particle gap to create an uncorrelated electron-hole pair. This difference will cause an influence on the wavelength of OLEDs emission.

1.2.5 Exciton relaxation: radiative and non-radiative processes

All the excitons, both singlets and triplets, generally are not long-lived (~ns for singlet excited state and ~ms for triplet excited state) in that they are forced to lose their energy within a period of time induced by quantum fluctuation, collapsing to their ground state radiatively or non-radiatively. All the possible ways of deactivation process of excitons are shown in the Jablonski diagram (Figure 1.14).

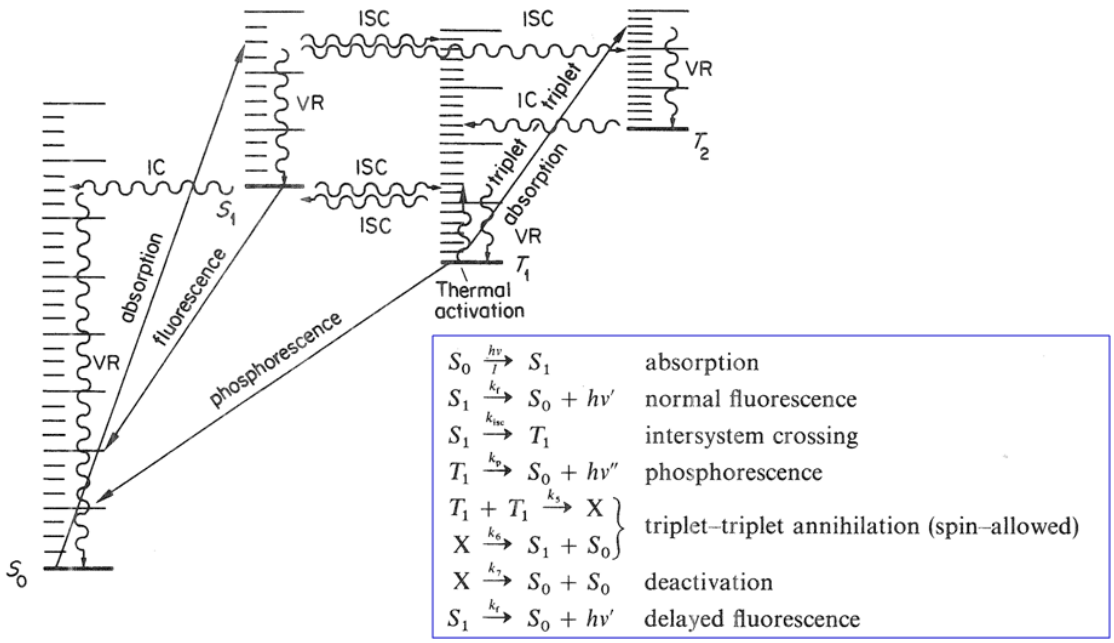

Figure 1.14: Jablonski diagram

A Jablonski diagram is a state energy diagram that shows the electronic transitions. Straight continuous lines represent the transitions involving absorption or emission of photons. Wavy lines represent the non-radiative transitions. In the figure, S_0 is the ground state, S_1 is the first singlet excited state, T_1 is the first triplet excited state, T_2 is the second triplet excited state, ISC is the intersystem crossing and IC is the internal conversion. All the different process can compete with each other over the deactivation of the excited state.

Non-radiative transitions include the internal conversion and the intersystem crossing. The internal conversion (Figure 1.15 (a)) is a process that the excited molecule dissipates its energy though a non-radiative transition, back to a lower energy state with the same spin multiplicity. This process, different from vibrational relaxation, is between two energy states. Internal conversion and fluorescence both are a process of deactivation of excited singlet. Internal conversion is an extremely rapid process, typically happen in $\sim 10^{-12}$ s. It does not only happen between S_1 state and S_0 state, but also happens between S_2 state and S_1 state, T_2 state and T_1 state, and other states with the same spin multiplicity. Because of the internal conversion, we can barely observe fluorescence from an excited singlet state above S_2 to the ground state S_0. Most of the fluorescence processes are transited from S_1 to S_0 state. The internal conversion and the fluorescence are two processes competing with each other. Therefore, a good fluorescence material is not only decided by the fluorescence rate (kf), but also controlled by the internal conversion rate (k_{IC}). As seen in Figure 1.15(b), the S_1 and T_1 state are overlapped. At the point of

intersection of the two states, the molecules can transfer from S_1 state to T_1 state. This is called intersystem crossing, a process that the excited molecule transfers to an energy state with different spin multiplicity though a non-radiative transition. The non-radiative deactivation from T_1 to S_0 is a process in competition with the regular phosphorescence.

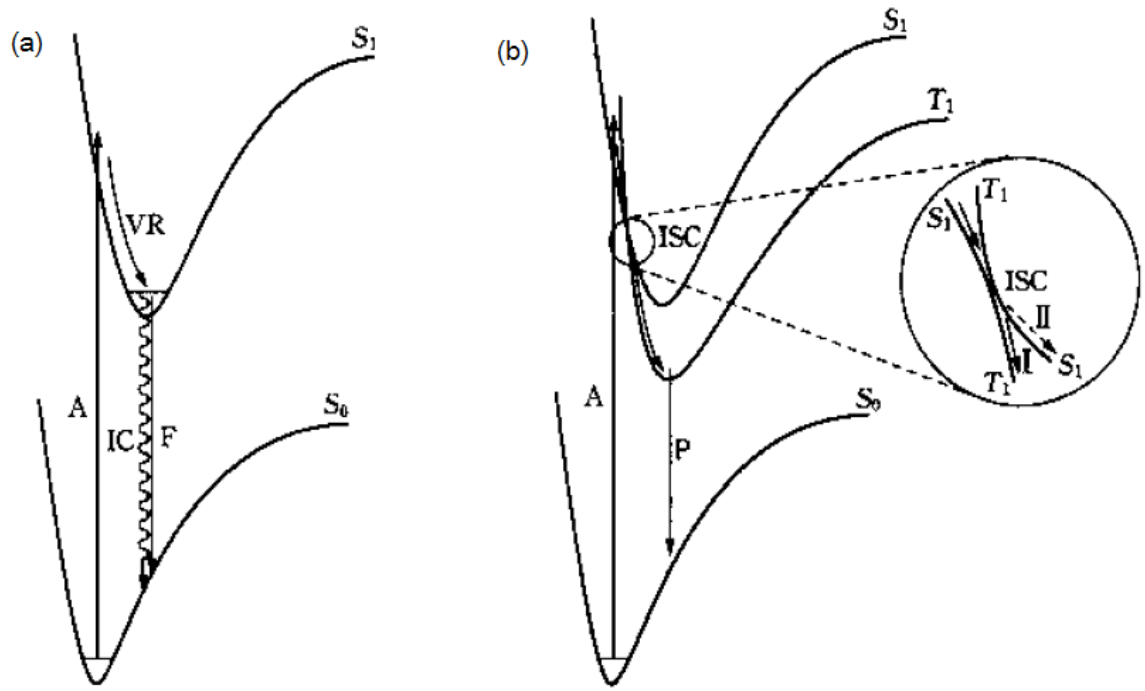

Figure 1.15: (a) Internal conversion and fluorescence, (b) Intersystem crossing and phosphorescence.

Radiative transitions include fluorescence and phosphorescence. Fluorescence, which is colored in green, results from a rapid radiative transition (~ns) between states of the same multiplicity. The transition is mainly contributed by the $S_1 \rightarrow S_0$ transition, although $S_2 \rightarrow S_0$ transition is occasionally observed and often hidden under a much more intense $S_1 \rightarrow S_0$ transition. Very weak $S_n \rightarrow S_m$ and $T_n \rightarrow T_m$ (n>m) fluorescence might be observed since they are spin allowed. Phosphorescence results from a transition between the states of different multiplicity, typically $T_1 \rightarrow S_0$ since $T_n \rightarrow S_0$ is very rare. Because phosphorescence is a transition which is a forbidden transition, it has much weaker intensities comparing with fluorescence. The triplet state always has lower energy than the corresponding singlet state (i.e. Energy of T_1 < energy of S_1). This is a consequence of the Hund's rule of maximum multiplicity. In situations where two unpaired electrons occupy different orbitals, there is a minimum energy of electron-electron repulsion when the spins are parallel. This repulsion energy will determine the energy difference between the excited singlet and triplet states depending on the extent of spatial overlap between

the orbitals involved. Therefore, in a material, light emission from phosphorescence will have a longer wavelength comparing with light emission from fluorescence. As mentioned earlier, the rate constant of phosphorescence can be dramatically increased by adding heavy atoms into the materials, which enables fast triplet dissipation due to the strong spin-orbital coupling.

Beside of radiative and non-radiative transitions, the energy of exciton can transfer to another exciton by emission and re-absorption of the photon, and by the electron and the hole transfer to a new molecule and form a new exciton, respectively known as Forster energy transfer and Dexter energy transfer. Forester energy transfer is a non-radiative transfer of energy due to dipole-dipole interaction between molecules in a long range of 30-100Å. This is a very fast process ($<10^{-9}$ s). Dexter energy transfer is also a non-radiative transfer of energy via the exchange of electrons between molecules by an electron hopping process with a much shorter range ~10Å. Dexter energy transfer occurs only between immediate neighbors where significant overlap between molecule wave functions can exist. Because Forster energy transfer is based on the photon emission and re-absorption, only singlet exciton is easier to form exciton by absorption of photons, and therefore only singlet exciton can have Forster energy transfer. However, Dexter energy transfer generally happens on triplet exciton.

1.3 Materials

As mention in the first section of this chapter, active organic materials can be often divided into two classes: small molecular materials and polymers. The fundamental properties of both classes are essentially the same: both have a conjugated π-electron system formed by the p-orbitals and sp^2-hybridized carbon atoms in the molecules. The sp^2-hybridized carbon atom is shown in Figure 1.16, in sp^2 hybridization, the 2s orbital is mixed with two of the three available 2p orbitlas to form three sp^2 orbitals with one remaining p orbital perpendicular to the plane of the hybrids. The 2s orbital and two 2p orbitals of different energies mix to form three new hybrid orbitals with the same energy which is determined by a weighted average of the atomic obitals that combined. In sp^2 hybridization, each sp^2 hybrid has 1/3 of s orbital character and 2/3 of p orbital character, and therefore the hybrid orbital sp^2 energy lies between that of the 2s orbital and the 2p orbital set (Figure 1.16).

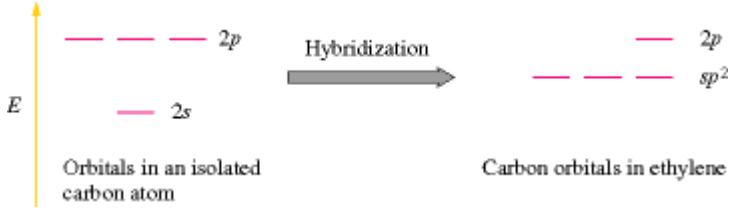

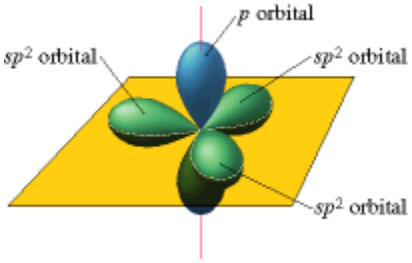

Figure 1.16: Sketch of the sp2 hybrid orbital, the upper figure shows the energy level of the sp2 hybrid orbital, the lower figure shows the spatial distribution of oribtals on a sp2 hybridized carbon atom.

The π-conjugated system occurs in an organic compound where atoms covalently bond with an alternating single and double bonds (e.g. C=C-C=C-C). The single bond is a σ covalent bond formed by two sp^2 hybrid orbitals belonging to two adjacent carbon atoms, and the double bond consist of two covalent bonds, one σ-bond which is the same as the single bond and one π-bond (Figure 1.17). Compared with the σ-bonds which form the backbone of the molecules, the π-bonds are significantly weaker. Therefore, the lowest electronic excitations of the conjugated molecules are the π-π*-transitions with an energy gap typically between 1.5 and 3 eV leading to the light absorption or emission in the visible spectral range. In the conjugated system, π-bonds overlap with the adjacent π-bonds, they influence each other to produce a region called electron delocalization. Electron delocalization region increases the stability of the molecule and thereby lowers the overall energy of the molecule. In this region, electrons do not belong to any single bond or atom but the molecule as a whole group. The overlaps of π-orbital allow electrons to move within the molecule, which shows the conducting property of the organic materials.

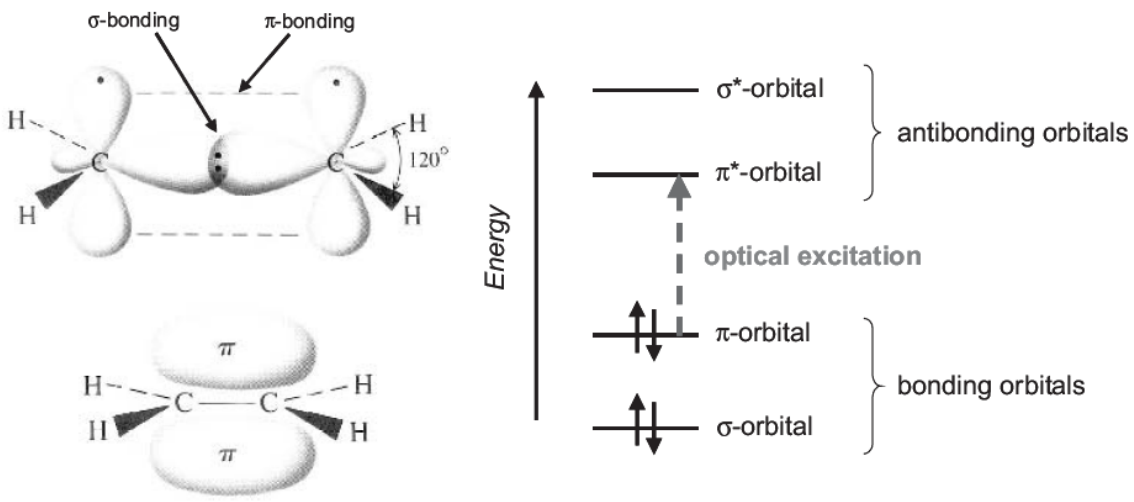

Figure 1.17: Left: σ- and π-bonds in ethene, as an example for the simplest conjugated p-electron system. The right viewgraph shows the energy levels of a p-conjugated molecule. The lowest electronic excitation is between the bonding π-orbital and the anti-bonding π*-orbital

In Figure 1.17, the π-orbital is the highest occupied molecular orbital known as HOMO, and π*-orbital is the lowest unoccupied molecular orbital known as LUMO. This is the energy diagram for a single ethane molecule. To compare the ethane material with the individual ethane molecule, the π-π stacking (caused by intermolecular overlapping of p-orbitals in π-conjugated systems) between the neighbouring molecules lead to more orbital split (see Figure 1.18). This orbital splitting produces sublevels of the HOMO and LUMO, and each of sublevels has its own energy slightly different from one another. There are as many sublevels as the molecules that interact with each other. When there are enough molecules influencing each other (e.g. in an aggregate), the number of the sublevels is large enough to be perceived as a continuum rather than discrete levels. Thus, we no longer consider them as discrete energy levels, but as continuous energy bands. The energy bands of the ethane (solid of liquid) have HOMO band and LUMO band, respectively. The energy difference of the HOMO band and the LUMO band is termed as band gap. The HOMO band of organic semiconductors is equivalent to the valence band of inorganic semiconductors. The same analogy exists between the LUMO band and the conduction band. All these features provide the organic materials similar semiconductor properties as the inorganic materials.

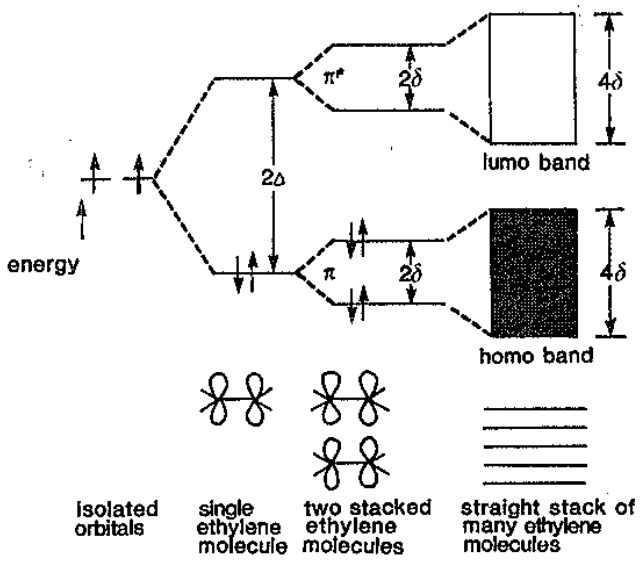

Figure 1.18: Overlap of π orbital electron wave functions lead to orbital split.

The divisions of organic materials are mainly depends on the ways that thin films are prepared. Small molecules are normally prepared by thermal evaporation in vacuum and polymers are processed from solutions.

1.3.1 Small molecules

Small molecules (Figure 1.19) are typically deposited from the gas phase by sublimation or evaporation. It does not mean that small molecular materials are not soluble. The solubility of small molecules can be increased by the synthetic addition of side chains. The OLEDs based on small molecular materials generally have higher efficiency comparing with PLEDs. It is because thermal evaporation process allows homogeneous organic thin film to form, better control during deposition, and complex multi-layer structures to form without damaging former layer. The drawback of thermal evaporation is the inefficient use of materials increasing the cost of fabrication. There are many alternative deposition methods to improve this shortcoming, such as organic vapor phase deposition (OVPD), and supersonic molecular beam deposition (SuMBD). All of them intend to control the vapor flow of materials in order to increase the efficiency of thermal evaporation.

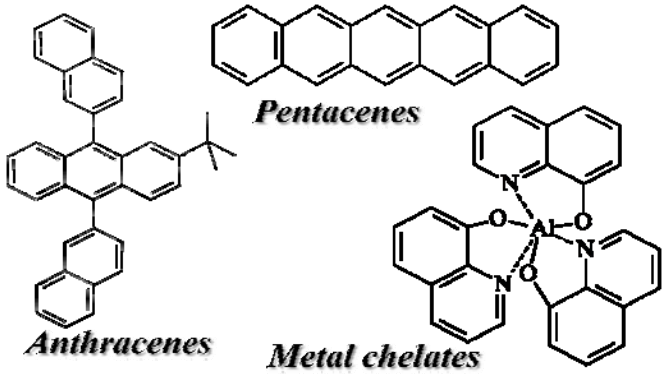

Figure 1.19: Example of small molecular materials

1.3.2 Polymers

Polymers (Figure 1.20) are typically prepared from solutions by spin-coating or printing techniques. The solution process is more suitable to form larger-area films than thermal evaporation, and it does not require the vacuum environment during the deposition. In addition, the inkjet printing allows simple direct fabrication of laterally structured circuitry, and enables large-volume roll-to-roll fabrication of organic devices. Thus, the solution process promises a lower fabrication cost which is the most attractive feature of organic semiconductor to electronics industry. However, the solution processes have their own disadvantages which is the deposition of subsequent layers tends to dissolve those layers already present. Thus, it is difficult to fabricate complex multilayer structure using the solution process. The controlled growth of the highly ordered and homogeneous films by solution processing is still an ongoing research area.

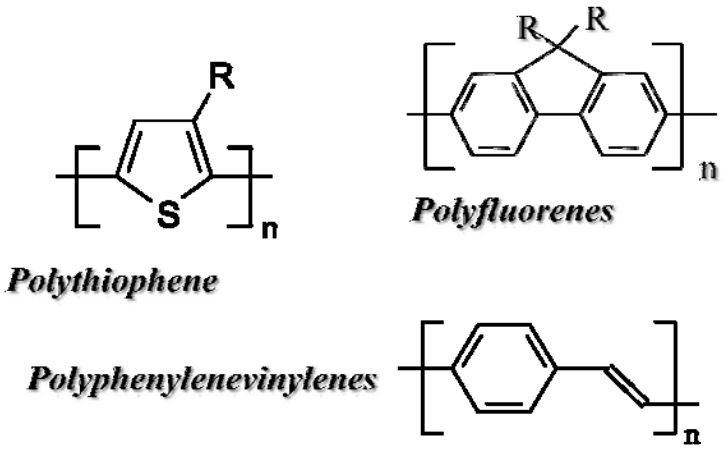

Figure 1.20: Example of polymer materials

1.3.3 Phosphorescent materials

Phosphorescent materials (Figure 1.21) are typically used as dopant in emissive layers of OLEDs, and they can be counted as small molecular materials. However, they are listing here as another category of organic materials because of the remarkable internal quantum efficiencies of phosphorescent OLEDs (PHOLEDs) (100% of internal quantum efficiency). As we can see in Figure 1.7, all the phosphorescent materials contain a heavy metal atom in their molecules. The heavy metal atom at the center of these molecules exhibits strong spin-orbital coupling, which is able to flip the electrons' spin direction. Consequently, the strong spin-orbital coupling facilitates intersystem crossing between singlet exciton state and triplet state. By doping phosphorescent materials in the emission layer of OLEDs, both triplet and singlet can recombine and emit photon, and achieve 100% internal quantum efficiency. The current problem of this highly energy efficient technology is that the lifetime of blue PHOLEDs is much shorter comparing with red and green PHOLEDs, which limit the PHOLEDs application as large screen displays and lighting sources.

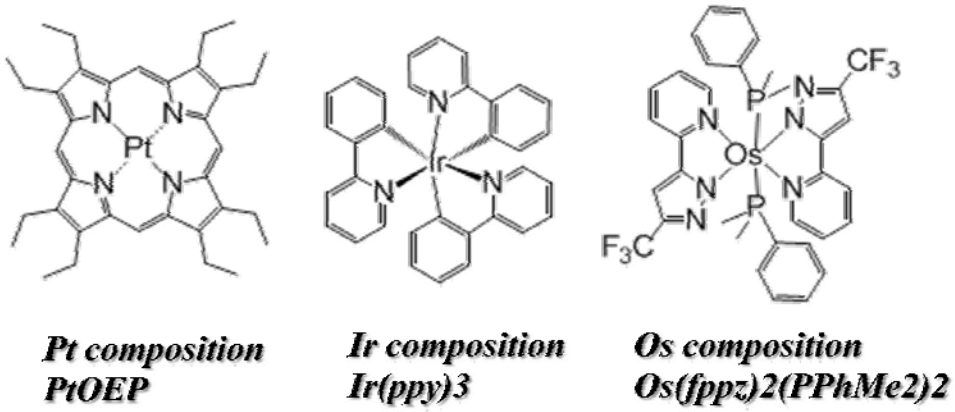

Figure 1.21: Example of phosphorescent materials

1.4 Transparent OLEDs

Among all the advantages of the organic semiconductors, organic light-emitting devices [7,8] (OLEDs) have attracted significant attention because of their great potential for making next-generation flat panel displays including transparent displays and mechanically flexible displays [51]. In particular, a display geometry in which the red, green and blue emitting devices are vertically stacked is a useful way to realize full color, high resolution image due to its simple fabrication process, small pixel size, and large fill factor offered by this architecture. Transparent OLEDs are essential in realizing this geometry as each OLED in the stack geometry has to be transparent to output the emitted light. Furthermore, transparent OLEDs can greatly improve the contrast, making it much easier to view displays under sunlight. Transparent OLEDs can also be widely applied to other facilities such as head-up display and smart windows.

1.4.1 Unique potential of OLEDs for enabling transparent displays

OLEDs have the great advantages of enabling transparent displays by nature, since most organic semiconductor materials are semi-transparent and able to emit light in visible region. As one can see from the emission and absorption spectrum of Alq_3 in Figure 1.22, most significant light absorption of Alq_3 is below 300nm which is not in the visible region. However, the emission light spectrum of Alq_3 is centered in 530nm in the visible region. This unique property of organic semiconductor is resulted from the luminescence band which is substantially red-shifted from the absorption band due to the characteristic Franck-Condon relaxation. Therefore, in general, the organic semiconductors are transparent in the visible region and able to emit visible light.

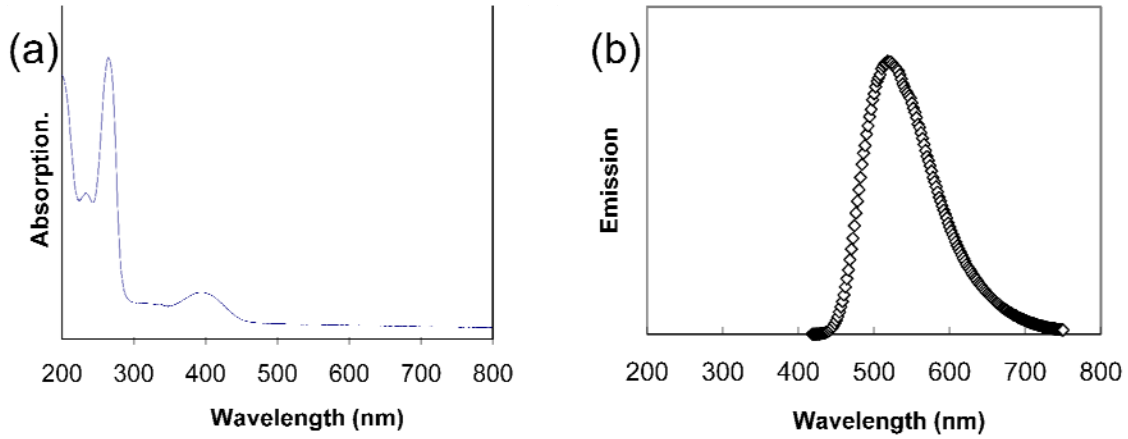

Figure 1.22: (a) absorption spectrum and (b) emission spectrum of Alq_3

Moreover, the deposition of organic semiconductors is a room temperature process, which makes organic semiconductors much easier to integrate with glass or plastic substrates. Especially, organic semiconductor solution processes, such as inkjet printing or roll-roll vapour deposition, theoretically make it cheaper to fabricate OLEDs.

1.4.2 Challenges with transparent OLEDs

Since organic semiconductors are normally transparent, the key of achieving transparent OLEDs is to have transparent electrodes. In conventional OLEDs, anode and cathode are using transparent ITO and nontransparent metal, respectively. Therefore, the critical component to achieve transparent OLEDs is to find the transparent cathode. Transparent cathode is critical for not only transparent OLEDs but also the top emitting OLEDs. The latter is important to the application of active-matrix displays with a high aperture ratio, which are impervious to driving circuits. Electroluminescence of the top-emitting OLEDs is extracted through a transparent top electrode instead of through the substrate and bottom electrode. In these OLEDs, a transparent cathode is necessary for the much more preferred "upright" OLED architecture (with the cathode as the top rather than the bottom, contact of an OLED) [52].

1.4.2.1 Transparent cathode

A transparent cathode is essential for transparent OLEDs intended for future "see through" electronics. To make transparent cathode, very thin films of Mg:Ag are first utilized as transparent cathodes[53-55]. However, Mg:Ag suffers from high chemical reactivity and poor electrical conductivity. In addition to Mg:Ag, researchers have examined ITO [56-59] as the cathode material due to ITO's high optical transmittance and low sheet resistance - around 85%

and 10Ω/□, respectively. However, the deposition of high quality ITO requires sputtering, a process that is not well-suited for fabrication of top electrodes, as the underlying organic layers subjects to damage by the plasma environment [60]. As such, protective layers are often introduced to reduce the damage to the underlying organic layers. However, this approach adds complexities to the fabrication process, and often alters and degrades device performance [61-66]. Alternative techniques for depositing ITO, such as ion-beam-assisted-deposition (IBAD) [67,68] are sometimes employed; however, the quality of ITO is usually compromised.

A dielectric/metal/dielectric multilayer structure was first reported in 1974 by Fan et al [69]. Bender et al. [70] and Fahland et al.[71] later reported that an ITO/Ag/ITO (IAI) multilayer electrode yields a higher optical transmittance and electrical conductivity than a conventional ITO electrode. The enhanced transparency of these structures arises from surface plasmon resonance (SPR) effects at the two metal/metal oxide interfaces [72]. Lewis and Grego [73] fabricated an OLED by growing an IAI anode through radio-frequency (RF) magnetron sputter deposition. However, damage to the organic layers during ITO sputtering remained a problematic issue. The highly transparent and conductive cathode, without damage underneath thin film during the deposition, is highly desired.

1.4.2.2 High efficient transparent OLEDs

Other than transparent cathodes, another challenge of transparent OLEDs is that the transparent TFTs cannot provide a lot of current to the transparent OLEDs due to the low carrier mobility. With not enough current, the light emission of transparent OLEDs cannot meet the required brightness for displays application.

1.4.3 Strategy to achieve high performance transparent OLEDs

As mentioned above, there are two primary challenges to achieve high performance transparent OLEDs: high quality transparent cathodes without causing damage to the underneath organic thin films, and no enough current provided by transparent TFT. For transparent cathode, ITO/Ag/ITO is a good candidate for transparent cathode due to the advantages in transmittance, sheet resistance and mechanical flexibility. However, the damage to the organic layers during ITO sputtering remained a problematic issue. To circumvent this issue, there has been a growing interest in developing transparent multilayer electrodes that can be deposited by simple thermal evaporation. To this end, thermally-evaporable WO_3/Ag/WO_3 [74] and ZnS/Ag/ZnS [75,76] transparent multilayer electrodes were recently developed, which exhibited optical transmission greater than 80% and sheet resistance below 10Ω/□. However, WO_3 and ZnS have high melting

temperatures (T_m) (1473℃ and 1830℃, respectively) and hence need to be evaporated at high temperatures. Transparent multi-layer electrodes which have a low sheet resistance, high optical transparency, and can be thermally evaporated at lower temperatures, are highly desired.

For the problem of not enough current provided by transparent TFT, one way to solve this problem is to increase the efficiency of transparent OLEDs, and then the transparent OLEDs will be able to maintain the acceptable brightness with the limited current provided by the transparent TFT, another way is improving the performance of the transparent TFT. However, this work is mainly focus on the transparent OLEDs, so we intend to solve this problem by improving the OLEDs efficiency. As we mentioned in the operation mechanism of OLEDs, using carrier injection layers or increasing the conductivity of charge transport layers can increase the OLEDs efficiency. As in line with the idea of using dielectric/metal/dielectric stack as transparent cathode, exploring dielectric material with efficient carrier injection and transport is following a logical train of thought to achieve high efficient transparent OLEDs.

1.5 Objectives and approaches

1.5.1 Objectives

In this work, MoO_3 is investigated for utilization as a transparent MoO_3/Ag/MoO_3 (MAM) stack cathode and as a charge transport material in form of MoO_3 and hole transport material mixture in transparent organic light emitting devices.

1.5.2 Approach and Rationale

1.5.2.1 The reason for using MoO_3

As mentioned above, transparent multi-layer electrodes with low sheet resistance and high optical transparency, which can be thermally evaporated at lower temperatures, are highly desired. Although many dielectric/metal/dielectric multilayer structures can be thermally evaporated, such as WO_3/Ag/WO_3 and ZnS/Ag/ZnS, the relatively high T_m makes them less interesting. However, the T_m of MoO_3 is only 795℃, which allows the MAM cathode to be readily fabricated using thermal evaporation at much lower temperatures and safely deposited on top of organic layers without thermal damage. This is the advantage of using MoO_3 as dielectric materials of a stack cathode. However, the challenge comes from how to successfully integrate MAM stack as a cathode in real OLEDs. The use of MAM electrode as a hole-collecting contact (i.e. anode) in an organic solar cell has been recently reported [77]. However, its use as an electron-injecting contact (i.e. cathode) in an OLED (or any other organic device), has not - to the best of our knowledge - been reported. This may be due to the fact that MoO_3 is well known to facilitate hole

injection [78- 84], which makes its successful use as an electron injecting contact rather unexpected.

Nevertheless, our studies in section 3.1 show that it is possible to achieve efficient electron injection from MAM electrode into organic layers by means of incorporating a suitable electron injection layer (EIL) at the interface. Therefore, MAM stack not only shows high transmittance and low sheet resistance, but also shows the potential to integrate as the cathode in real transparent OLEDs.

To achieve high efficient transparent OLEDs, a carrier injection layer or high carrier transport materials are desired. Due to its benefits on device performance, the use of MoO_3 as a hole injection and/or transport material in organic light emitting devices (OLEDs) and organic solar cells (OSCs) has gained momentum rapidly in recent years. In the case of OLEDs, its use a hole injection layer [85- 89] , or as a dopant [90- 94] in the hole transport layer, can lower the driving voltage and improve the stability [95-97]. The use of OSCs, its use as an anode buffer layer proved beneficial to power conversion efficiency [98,99]. Its high optical transmittance, low evaporation temperature, and the fact that it can be doped into organic semiconductor materials at high concentrations (~50%) without negatively impacting charge transport [97,100] have spurred the interest in studying it in mixtures with charge transport materials [97,101]. Therefore, MoO_3 is not only a good candidate of the transparent cathode, but also able to improve device efficiency by acting as an injection layer and a high conductive layer.

However, the conductivity of MoO_3 and carrier transport material mixture is not well understood. Shin et al [97] showed that doping N,N′-bis(naphthalen-1-yl)-N,N′-bis (phenyl)benzidine (NPB) with MoO_3 resulted in higher conductivity, and attributed the effect to charge transfer between MoO_3 and NPB. Their C-V measurements showed that the carrier density in MoO_3:NPB mixtures was several orders of magnitude higher than that in neat NPB, and was also higher than that in neat MoO_3. Although there was no direct experimental verification, the higher charge density suggested the mixture could have higher conductivity in comparison to MoO_3. Ma et al [101] also observed that the conductivity of NPB increased rapidly on doping with MoO_3. Interestingly however, and at odds with findings by Shin et al, they found that the trend saturates at higher MoO_3 concentrations, limiting the conductivity of mixtures with high MoO_3 concentration (> 30%) to that of neat MoO_3. In view of the tremendous growth and potential of the organic electronics industry, and the emergence of MoO_3 as an important enabling material, resolving this apparent discrepancy between the findings of the two studies becomes a matter of high scientific interest and technological importance.

In the section 3.2 of this thesis, we systematically investigate the conductivity of thin films of mixtures of MoO_3 and hole transport materials (HTM) as a function of MoO_3 concentration. In order to better resolve and differentiate between the contributions from the injection and bulk transport, the materials are studied in lateral devices in addition to the more conventional vertical device configuration. The results show that mixing MoO_3 with a hole transport materials, such as NPB or 4′,4″-tri(N-carbazolyl)triphenylamine (TCTA) brings about >5 orders of magnitude increase in bulk conductivity over that of neat MoO_3 or neat HTM film. The results also show that the mixing film enhances both hole and electron transport. The findings shed the light on the potential of hybrid composites of inorganic and organic materials in realizing enhanced conductivity.

In general, the low T_m of MoO_3 allows fabricating high quality transparent MAM stack cathode, and mixing MoO_3 and HTM reveals the potential of MoO_3 to act as a high conductivity carrier transport material. It makes MoO_3 particularly interesting in transparent OLEDs application.

1.5.2.2 The reason for using small molecule OLEDs

In this work, all the OLEDs materials are small molecules and deposited from the gas phase by conventional thermal evaporation. This is because the OLEDs based on small molecular materials generally have higher efficiency comparing with PLEDs, and thus high performance OLEDs studied and fabricated in research lab are generally all based on small molecule materials. Moreover, the OLEDs structures in this work are relative complex and include dopant in the emitting layer and the carrier injection layer. And thermal evaporation process of small molecule materials allows homogeneous organic thin film to form, better control during deposition, and complex multi-layer structures to form without damaging the former layers. Therefore, using small molecule OLEDs in this study is the best choice, but also the only choice.

1.6 Thesis Organization

In this work, MoO_3 is investigated for utilization as a transparent MoO_3/Ag/MoO_3 (MAM) stack cathode and as a charge transport material in form of MoO_3 and hole transport material mixture in transparent organic light emitting devices. The thesis organization is concluded as follow.

Chapter 1 is the introduction of OLEDs including OLEDs history and background, OLEDs structure and operation mechanisms, OLEDs materials, transparent OLEDs and the objective and approach of this thesis. The focus of this chapter is the structure and operation mechanisms of

OLEDs, dividing into four sections: carrier injection, carrier transport, exaciton formation, and decay of excitons.

Chapter 2 is the experiment detail regarding to the author's work including device structure, device fabrication and device testing.

Chapter 3 is the result and discussion including three sections: transparent OLEDs using MAM cathode, enhanced bulk conductivity and bipolar transport in mixtures of MoO_3 and organic hole transport materials.

Chapter 4 is the conclusion.

Chapter 2

Experiment

Experimental details including device structures, device fabrication and device testing are explained in this chapter. Device structures include the standard vertical structure and the lateral structure, employed in section 3.1 and section 3.2 of this thesis, respectively. All the devices are fabricated by conventional thermal evaporation of small molecule materials. All the devices are stored and tested in a nitrogen atmosphere and at room temperature.

2.1 Device structures

In the work of transparent OLEDs using MAM cathode, firstly, MAM configurations of the general structure MoO_3(*x* nm)/ Ag (*y* nm)/ MoO_3 (*z* nm), with $0 < x < 40$nm, $10 < y < 20 < 40$nm, $0 < z < 40$nm are studied. Secondly, the transparent OLED structure used in the experiment consists of ITO(100nm)/ N,N′-bis(naphthalen-1-yl)-N,N′-bis (phenyl)benzidine(NBP) (70nm)/ tris(8-hydroxyquinoline) aluminum (Alq_3) : 10-(2-benzothiazolyl)-1, 1, 7, 7-tetramethyl-2, 3, 6, 7-tetrahydro-1*H*, 5*H*, 11*H*, [*l*] benzo-pyrano [6,7,8-*ij*] quinolizin-11-one (C545T) (99.2%:0.8%) (30nm)/ Alq_3 (30nm)/ 4,7-diphenyl-1,10-phenanthroline (Bphen) : (Cs_2CO_3) (9:1) (10nm) / MoO_3(*x* nm)/ Ag (14nm)/ MoO_3 (40nm), where NPB and Alq_3 serve as a hole transport layer and an electron transport layer, respectively, Bphen: Cs_2CO_3 (10%) is the electron injection layer , (Alq_3):C545T(0.8%) is the emitter layer, and the multilayer of MoO_3 (*x* nm)/Ag (14nm)/MoO_3 (40nm) is the cathode, see Figure 2.1 (a).

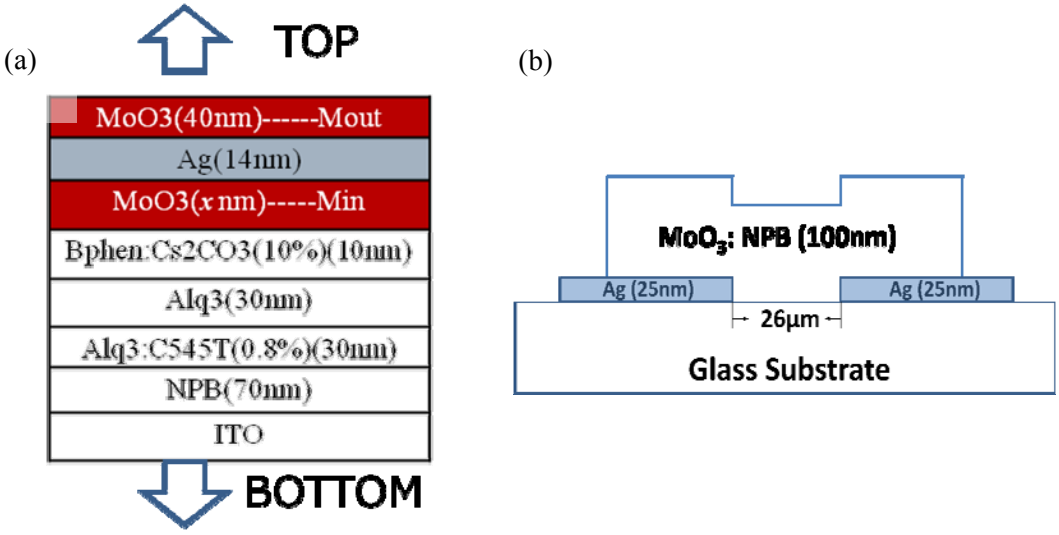

Figure 2.1: Devices structures: (a) Vertical structure; (b) Lateral structure.

In the work of enhance bulk conductivity of MoO_3 and organic HTM mixtures, for comparing conductivity of thin films of MoO_3, HTM and MoO_3:HTM mixtures of various MoO_3 concentrations (x %, by volume), test devices of two different structures, fabricated on glass substrates, are employed: (1) a standard vertical structure in which a ~100 nm thick layer of the material to be tested is sandwiched between ITO and Ag (or Mg:Ag) electrodes, and (2) an unconventional lateral structure in which a ~100 nm thick layer of the material is coated onto two Ag electrodes (~25 nm thick) , both pre-coated on the same substrate, and separated by a ~26 μm gap. In the standard vertical structure, the device consists ITO/ 100nm of NPB or MoO_3, or NPB: MoO_3 (50%) mixture/ Mg:Ag (9:1) (60nm)/ Ag (60nm). In the lateral structure (Figure 2.1(b)), pure NPB, pure MoO_3, and NPB: MoO_3 (x %) mixture with different MoO_3 composition ($0 \leq x \leq 100$) were deposited to bridge the Ag gap in test devices. To grow the mixture layer, MoO_3 and NPB were co-evaporated from different sources in a same chamber. Similar devices with 4′,4″-tri(N-carbazolyl)triphenylamine (TcTa) and MoO_3 mixture were also fabricated and tested. To examine the hole transport property of the mixture material, a vertical structure (hole-only device) consisting of ITO/ NPB (100nm)/ NPB or MoO_3:NPB (50%) (100nm)/ NPB (100nm)/ NPB: 2,3,5,6-tetrafluoro-7,7,8,8-tetracyanoquinodimethane (F_4-TCNQ) (9:1) (10nm)/ Mg:Ag (9:1) (60nm)/ Ag (60nm) (Figure 2.2(a)) was grown and tested. To examine the electron transport property of the mixture material, a vertical structure (electron-only device) consisting of ITO/ Mg (2nm)/ Alq_3 (40nm)/ Alq_3 or MoO_3:NPB (50%) (40nm)/ Alq_3 (40nm)/ Mg:Ag (9:1) (60nm)/ Ag (60nm) (Figure 2.2(b)) was grown and tested.

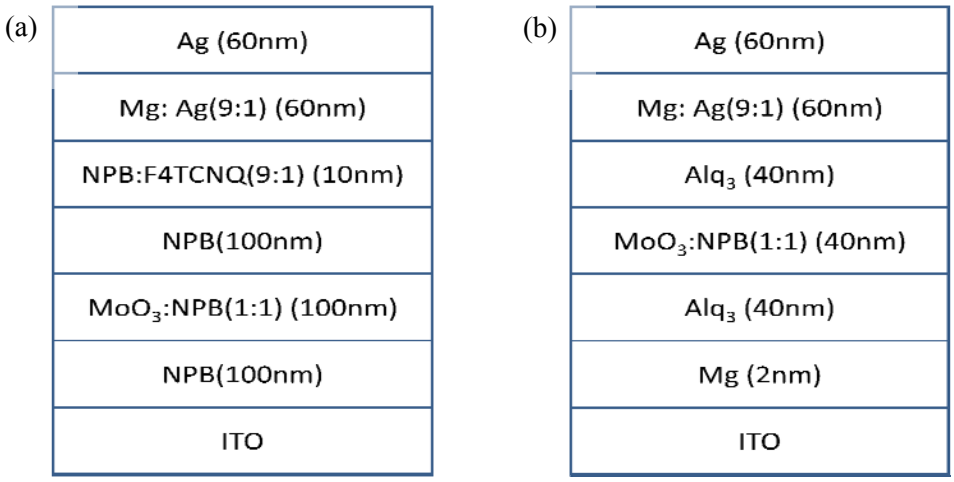

Figure 2.2: Vertical structures (a) hole-only device; (b) electron-only device

More details of the device structure are described in the corresponding sections of chapter 3.

2.2 Device fabrication

All the devices are fabricated on ITO coated glass substrate by thermal evaporation of small molecule materials.

2.2.1Substrate preparation

Glass substrate with ITO patterned anode is used in all of our devices. The ITO surface has an important influence on the device performance. Here are the steps used to clean the ITO substrate.

1. ITO substrates are put into 1L beaker filled with Acetone and cleaned with ultrasonic bath for 15 minutes to remove all kinds of organic contaminations on the ITO substrate surface.
2. Clean the ITO substrate with Q-tips to remove any contaminations sticking on the surface.
3. Put ITO substrate back in the beaker filled with Isoproponal, and cleaned with ultrasonic bath for another 15 minutes.
4. Use nitrogen gun to dry the ITO substrates and blow away any particles.
5. Put ITO substrate into an oven at 90℃ for 15~20 minutes to remove the moisture on the ITO substrate.
6. Use reactive ion etching (RIE) to give a plasma treatment to the ITO substrate. RIE forms a thin film which improves the work function of ITO, as the surface treatment we mentioned in the charge injection section in chapter 1. The surface plasma treatment is exactly how we improve the charge injection and the device lifetime.

   The parameters of RIE treatment is:

   Pressure: 20 torr

   Inductive Coupled Plasma (ICP) Power: 20

   Duration: 2min

   Chemical: CF_4 - 15 torr

   O_2 - 5 torr
7. Immediately put the clean ITO substrate into thermal evaporation chamber and vacuum the chamber.

2.2.2 Thin film deposition by PVD

All materials are deposited sequentially at a rate of 1-3 Å/s using conventional vacuum thermal evaporation at a pressure below 5×10^{-6} Torr, by Intelvac OLED system OLED6T2E10S (Figure 2.3 (a)) and Angstrom EVOVAC Deposition system 00903 (see Figure 2.4 (a)). This work uses both of the OLED systems.

The Intelvac OLED system is designed for dual chamber evaporation (thermal evaporation and e-beam evaporation) in a high vacuum load-lock with material handing in an atmosphere-controlled glovebox. In this work, the transparent OLEDs were fabricated in the thermal chamber of the Intelvac OLED system. The Intelvac system thermal chamber is the first chamber that is capable of evaporating by resistance evaporation from six different evaporation sources (Figure 2.3 (b)). The thickness of the deposited film is monitored by the controller based on the feedback from the crystal sensor assigned to each individual source. Two separated controller allows two materials mixing by co-evaporation. For the complex multilayer transparent OLED structure in this work, the Intelvac system allows the whole fabrication process protected under nitrogen environment all the time, which avoids any device degradation during fabrication process.

(a) (b)

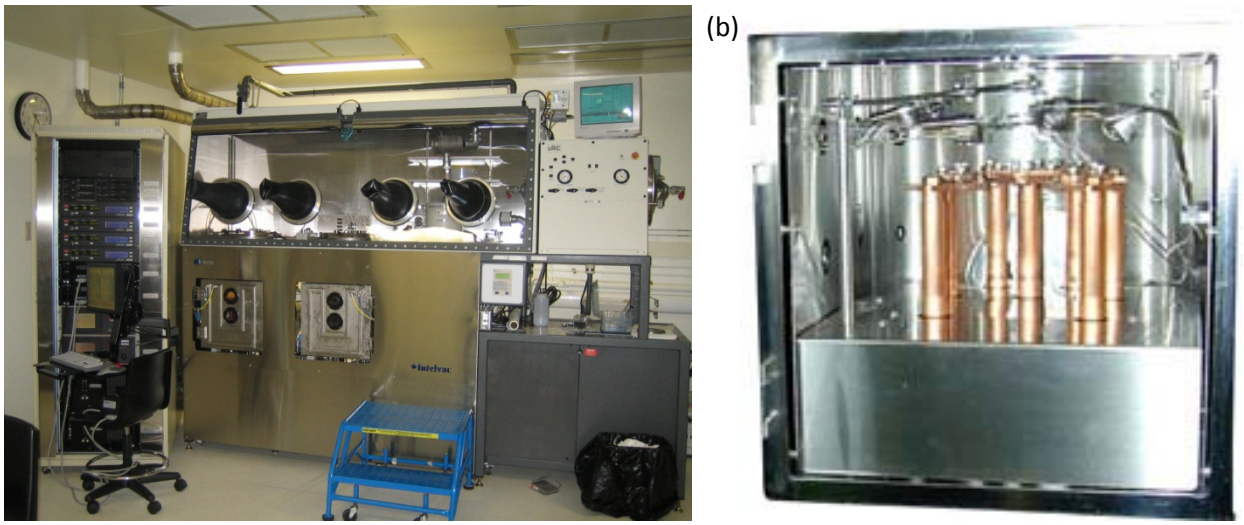

Figure 2.3: (a) The Intelvac OLED system OLED6T2E10S (b) The inside look of the thermal chamber

The Angstrom EVOVAC Deposition system is capable of combining multiple thin film deposition sources, using up to ten thermal evaporation sources, electron beam evaporation, and four magnetron sputtering target, in the same chamber (Figure 2.4 (b)). In this work, all the MoO_3 and organic material mixture thin film were fabricated only using the thermal evaporation sources of the Angstrom EVOVAC Deposition system. Since the Angstrom EVOVAC Deposition system

has 10 thermal evaporation sources which are controlled by 4 outputs and are monitored by 4 crystal sensors, we can mix up to 4 different materials by co-evaporation. This advantage of the system is critical to investigate the electrical and optical properties of the mixture films.

(a) (b)

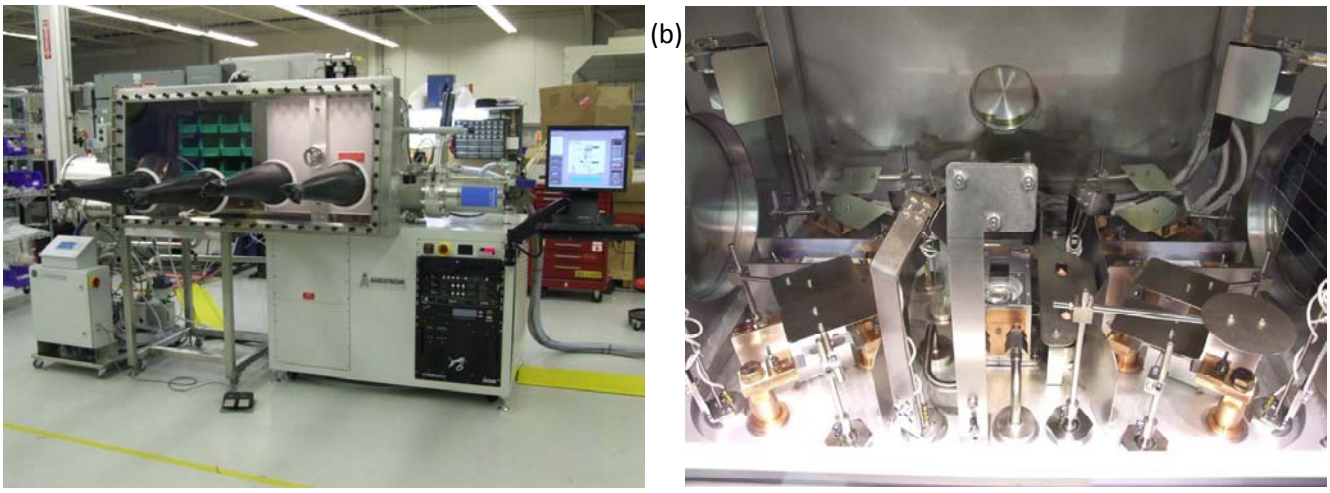

Figure 2.4: (a) The Angstrom EVOVAC Deposition system 00903 (b) The inside look of the chamber

2.4 Device testing

After the device fabrication, all the testing and measurements of OLEDs are carried out in a nitrogen atmosphere and at room temperature. During the testing, devices are installed in testing box with nitrogen flowing through to prevent the ambient degradation. Between different testing, the devices are also stored in a metal storage box with nitrogen flowing through the box all the time. Primary testing, measurements, and the equipments used in this work are listing below.

The optical transmittance and electrical conductivity of the MAM are measured by using Shimadzu UV-2501PC UV-Visible spectrophotometer (Figure 2.5) and two point probe method, respectively. The surface morphology of the MAM is verified with a Digital Instruments Dimension 3100 atomic force microscope (Figure 2.6). The current density (J)-luminance (L)-voltage (V) characteristics of the device is measured with Agilent 4155C semiconductor parameter analyzer (Figure 2.7) and a silicon photodiode which is pre-calibrated by a Minolta Chromameter CS-100A (Figure 2.8).

Figure 2.5: Shimadzu UV-2501PC UV-Visible spectrophotometer

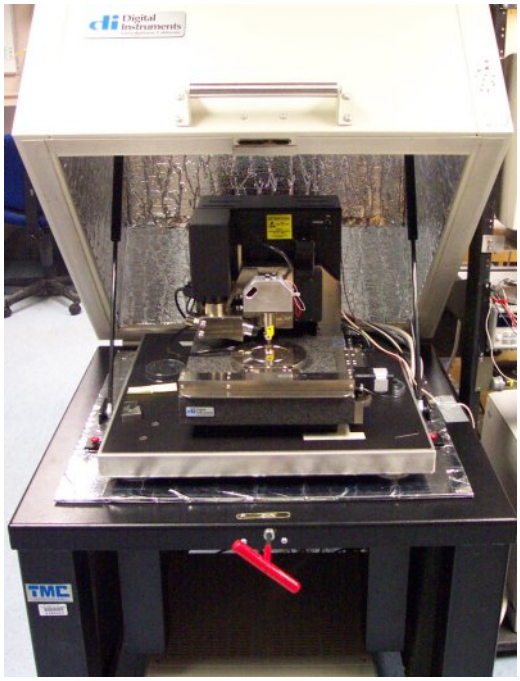

Figure 2.6: Digital Instruments Dimension 3100 atomic force microscope

Figure 2.7: Agilent 4155C semiconductor parameter analyzer

Figure 2.8: Minolta Chromameter CS-100A

Chapter 3

Results and Discussion

The experiment results of the investigation of MoO_3 for utilization as a transparent cathode and as a charge transport material in transparent organic light emitting devices are shown in this chapter. The discussion of the device performance as well as the observed phenomenon is explained in detail in corresponding sections.

3.1 Transparent Organic Light-emitting Devices using a MoO_3/Ag/MoO_3 Cathode*

Transparent OLEDs is one of important application of organic semiconductor. Transparent OLEDs have great application potential in active-matrix displays, see-through displays, auto navigation systems, etc. In Transparent OLEDs, a transparent cathode is necessary for the much more preferred "upright" OLED architecture. A dielectric/metal/dielectric stack structures show a high transmittance in visible region due to the SPR effect and fair electrical conductivity, which was employed as transparent cathode in this work. Most common seen dielectric/metal/dielectric stack is ITO/Ag/ITO stack [70,71,73], however, deposition ITO on top of organic semiconductor is harmful to underneath organic layers. So other thermally-evaporable stacks such as WO_3/Ag/WO_3 [74] and ZnS/Ag/ZnS [75,76] have been introduced by other researchers. In this work, we investigate MoO_3/Ag/MoO_3 (MAM) stacks for utilization as transparent cathodes in OLEDs, because of MoO_3 have lower melting temperature and comparable optical and electrical performance comparing with other stacks (WO_3/Ag/WO_3 or ZnS/Ag/ZnS).

3.1.1 Optimized MAM stack

Just like many other researches on dielectric/metal/dielectric stack structures, the electrical and optical properties of the MAM stack alone are the very first things to investigate.

Figure 3.1(a) shows the transmittance spectra of (i) MoO_3 (~40 nm thick) single layer (curve A); (ii) MoO_3 (~40 nm thick) / Ag (~16 nm thick) bi-layer structure (curve B); and (iii) MoO_3 (~40 nm thick) / Ag (~16 nm thick) / MoO_3 (~40 nm thick) MAM stack (curve C); all formed on a glass substrate and fabricated in a single growth process by using shadow mask. Figure 1(a) (curve A) shows that a single 40 nm thick MoO_3 is quite transparent over a wide wavelength range (400 - 900 nm). With an additional 16 nm Ag layer on top of it, the transmittance drops

* The main content of this section was submitted and accepted by Journal of Applied Physics.

significantly down to 20%-50% (curve B). Nevertheless, after adding a second 40 nm thick MoO_3 layer, the film transmittance increases to 50-70% (curve C). The high optical transmittance of the MAM stack clearly verifies the presence of non-linear optics, which can be attributed to surface plasmon resonance effect. Figure 3.1(b) shows corresponding AFM images of the surfaces of the three configurations. The root mean square for surface roughness value are found to be 0.581nm, 3.020nm and 0.900 nm for surfaces A, B and C respectively, showing that MoO_3 forms very smooth films, and that the top MoO_3 layer "levels out" the relatively rougher texture of the Ag layer.

(a)

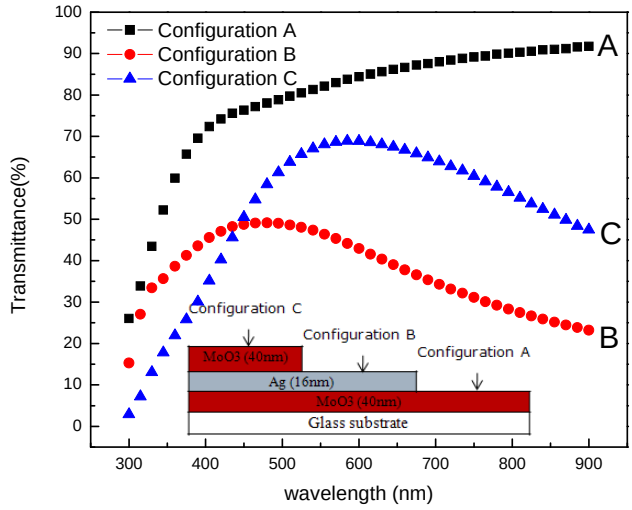

(b)

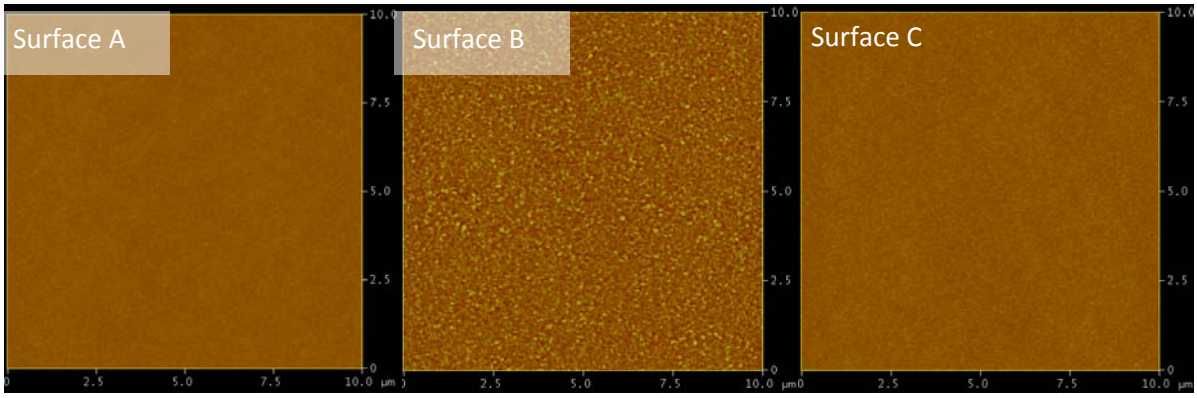

Figure 3.1: (a) Optical transmittance of three different layer configurations: A: MoO_3 (40 nm) single layer; B: MoO_3 (40 nm)/Ag (16 nm) bi-layer; and C: MoO_3 (40 nm)/Ag (16 nm)/ MoO_3 (40 nm) MAM. Inset: a schematic diagram of the three configurations. (b) Atomic force microscope (AFM) images of the surfaces of each configuration: RMS roughness values are 0.581nm, 3.020nm and 0.900nm for configurations A, B and C respectively.

The thickness of the intermediate Ag layer is crucial in defining the optical and electrical properties of the MAM stack. Figure 3.2(a) shows the optical transmittance of the MAM stack with varying Ag layer thicknesses (12 – 20 nm). As expected, the film transmittance gradually decreases on increasing the thickness of the intermediate Ag layer. To achieve a higher optical transmittance, the Ag layer thickness should be kept as thin as possible. Figure 3.2(b) shows the sheet resistance of the MAM stack, showing, as expected, that the stack becomes more conductive as the Ag layer thickness increases. At an Ag layer thickness of ~14 nm, the sheet resistance roughly saturates at 9Ω/□ which is on par with that of ITO. Based on this observation, the Ag layer thickness of the MAM structure that is incorporated in the transparent OLEDs is set to 14 nm. At this Ag thickness, the MAM transmittance is 65%-80% in the visible range (i.e. 400-700 nm range).

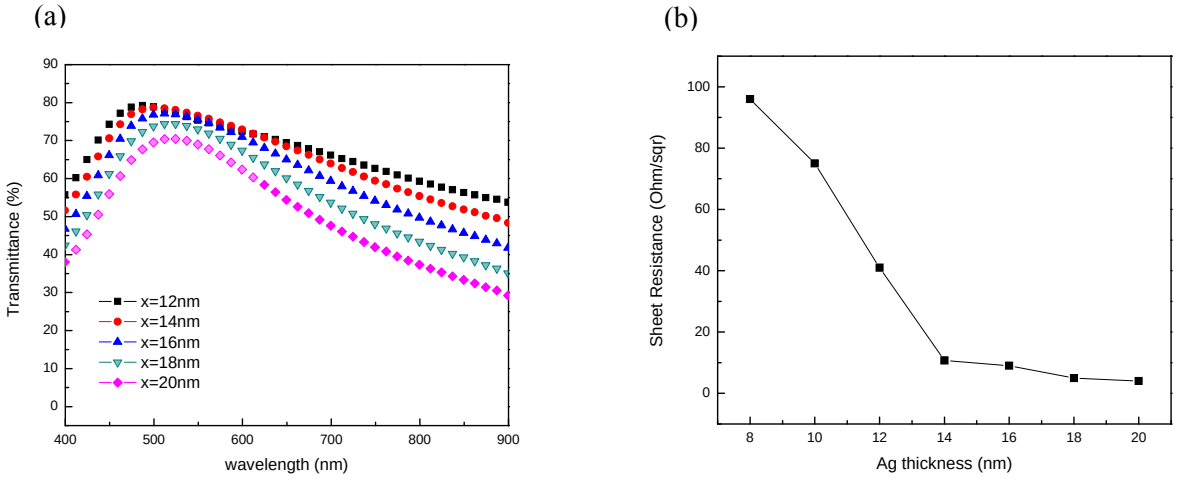

Figure 3.2: Optical transmittance (a); and sheet resistance (b) of MoO_3 (40nm)/Ag (*x* nm)/MoO_3 (40nm) multilayer structures on glass, with *x* varying from 12nm to 20nm.

3.1.2 Integrated MAM cathode with real OLEDs

To investigate using MAM as transparent cathode in real OLEDs, efficient electron injection from MAM stack to the electron transport layer is crucial. However, efficient hole injection from MoO_3 into organic hole transport layers has been reported [78-84] and a MAM multilayer was successfully utilized as an anode in an organic solar cell [77]. Our observations show that although electron injection from a MAM stack into an organic electron transport layer (ETL) is rather poor, efficient injection can be achieved by means of incorporating a thin EIL. To find the proper EIL spent the author a significant amount of time, we have tried most of the commonly used EIL, such as Cs_2CO_3, Mg, Mg:Ag, MoO_3:Ag, and Bphen, and all of these EIL did not

provide good electron injection to achieve high performance device. To slide over finding proper EIL, author also tried inverted OLEDs structure (i.e. anode on top of the device) to use MAM as transparent anode. However, the devices performance is still poor, a total luminance of 150 cd/m^2 at 8V under 20 mA/cm^2 constant current density.

At last we tried Bphen doped with Cs_2CO_3 as EIL, it is known that alkali metal dopants can significantly improve the electron injection efficiency [102,103]. In our experiments, we use a ~10 nm EIL made of Bphen: Cs_2CO_3(5%) in-between the MAM cathode and the Alq_3 ETL (see Figure 3.3 left). Results show that it is possible to achieve efficient electron injection from MAM electrode into organic layers by means of incorporating this 10nm EIL of Bphen: Cs_2CO_3(5%) at the interface. The best device performance is: at the constant current density of j = 20 mA/cm^2, the device bias is 7.3 V, the bottom luminance is 307cd/m^2, the top luminance is 84cd/m^2 and the whole device shows a peak transmittance about 85%.

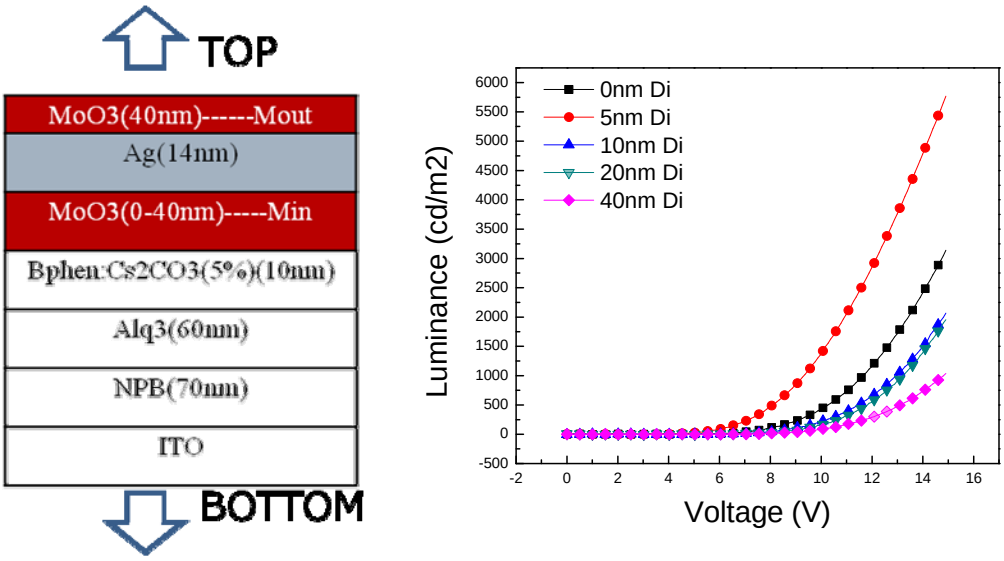

Figure 3.3: Left: Schematic layer structure of the transparent OLED with a MoO_3(x nm)/Ag (14nm)/MoO_3 (40nm) cathode. Right: luminance-voltage characteristics of the OLEDs with different inner MoO_3 (M_{in}) thicknesses.

To further improve the OLEDs' performance, we introduce dopant C545T in the EL. A series of transparent OLEDs are fabricated and tested to optimize the device performance on the dopant concentration. The results show that the devices with EIL of Bphen: Cs_2CO_3(10%) and EL of Alq_3:C545T (0.8%) have the lowest driving voltage and the highest luminance under the constant current density 20 mA/cm^2.

To study MAM's functionality as cathodes in transparent OLEDs, we fabricate and test a series of transparent OLEDs with MAM cathodes that have identical optimized organic layer configurations based on the results from the dopant concentration optimization. In these devices, the thickness of the Ag layer and the outer MoO_3 (M_{out}) of the MAM is fixed (at 14 nm, and 40nm, respectively), whereas the thickness of the inner MoO_3 layer (M_{in}) is varied between 0 and 40 nm. Figure 3.4(a) shows the schematic layer structure of these OLEDs and Figure 3.4(b) presents their current density-voltage-luminance (J-V-L) characteristics. The luminance in Figure 3.4(b) represents the total luminance, which is the sum of the luminance measured from the top and bottom of one device. As shown in Figure 3.4, the device with M_{in} = 5 nm among the five exhibits the best performance. For example, at an injection current density of j = 20 mA/cm^2, the device bias is 7.2 V (the lowest) and the measured luminance is 1300 cd/m^2 (representing ~1000 cd/m^2 and ~300 cd/m^2 from the bottom and the top, respectively). The decrease in device turn-on voltage with decreasing M_{in} thickness can be readily explained in terms of the lower resistive losses across the thinner MoO_3 layer, and because the Cs-doped EIL can contact more directly with the intermediate Ag layer to form an ohmic contact at a thinner and non-continuous inner MoO_3 layer, thus leading to improved electron injection [102,103]. However, it is interesting to note that the device with M_{in} = 5 nm also shows a lower turn-on voltage than the one with no inner MoO_3 layer (M_{in} = 0 nm). This behavior may be attributed to the role of the thin oxide layer in improving electron injection via tunneling, by reducing the effective energetic barrier at the interface, as was observed with other metal oxides (Al_2O_3 [104], SiO_2 [105]) previously.

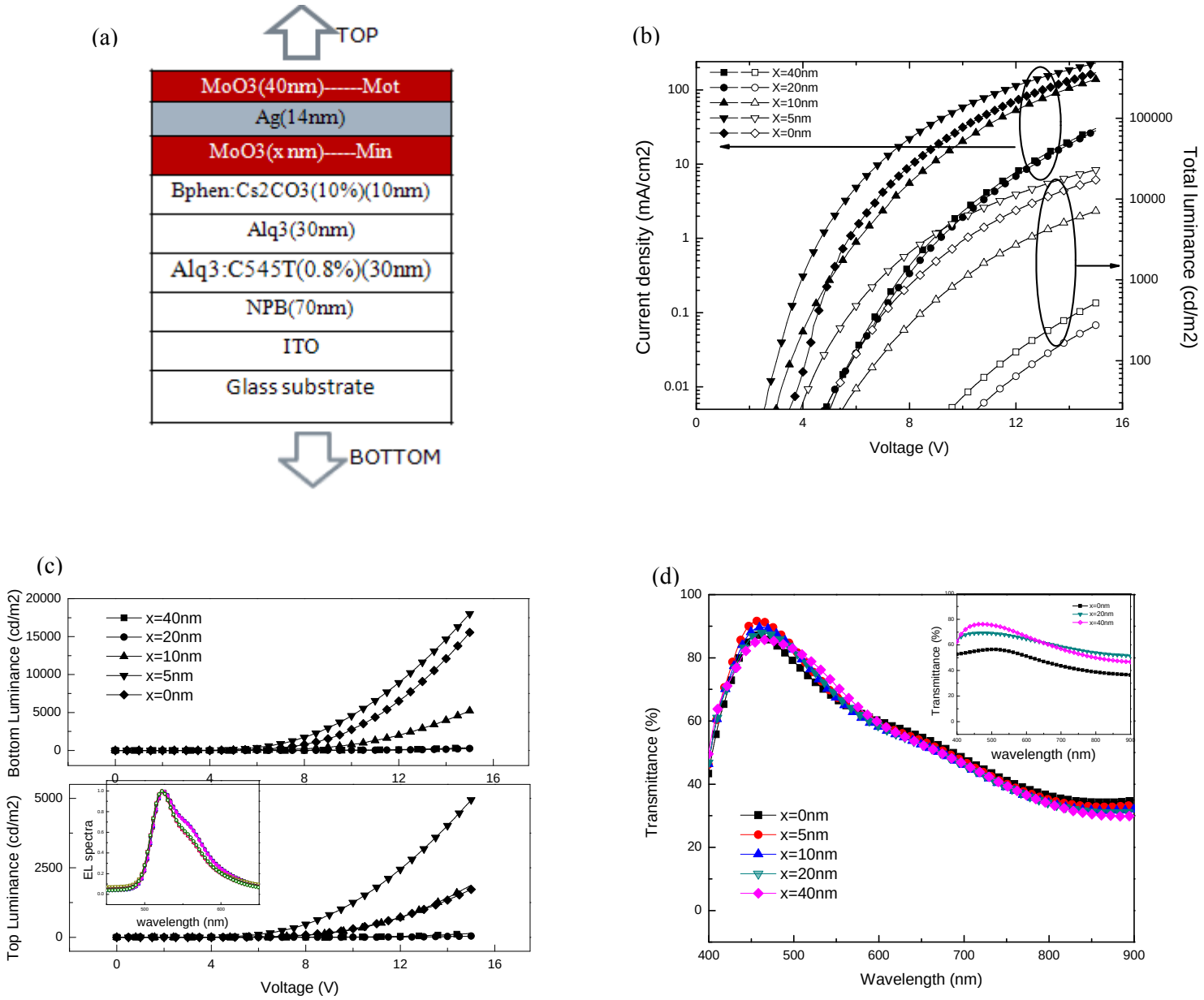

Figure 3.4: (a)Schematic layer structure of the transparent OLED with a MoO_3(*x* nm)/Ag (14nm)/MoO_3 (40nm) cathode. (b) The current density-voltage (J-V, solid symbols) and luminance-voltage (L-V, open symbols) characteristics (in Log scale) of the OLEDs with different inner MoO_3 (M_{in}) thicknesses. The reported luminance value is the sum of both top luminance and bottom luminance from one device. (c) The luminance-voltage curves measured from the top surface (open symbols) and the bottom surface (solid symbols) of the devices with different inner MoO_3 thicknesses. Inset: the electroluminescence spectra of the top emission (with smaller shoulder) and of the bottom emission (with larger shoulder) for each OLED device. (d) The transmittance spectra through all device layers for the OLEDs

with different inner MoO_3 thickness. Inset: the transmittance spectra of the MAM on glass with different inner MoO_3 thickness.

Figure 3.4(c) shows the top and bottom luminance components of the same OLEDs. Clearly, the bottom luminance is always higher than the top luminance for any device. This can be attributed to the fact that the optical reflection of the top MAM contact is higher than that of the bottom ITO contact. The ratio of the top to bottom luminance for the device with 5nm M_{in} is about 1/3, while the ratio is lower than 1/8 for the other four devices. The device with M_{in} = 5 nm exhibits more symmetric light emission than any other device. The inset of Figure 3.4(c) is the electroluminescence (EL) spectra of both top and bottom emission of the devices. All top-emission EL spectra peak at 522 nm with a weaker shoulder at 555 nm whereas all bottom-emission EL spectra show a peak at 525 nm with a slightly more prominent shoulder. The optical transmittance spectra of the five devices are shown in Figure 3.4(d). For comparison, transmittance spectra of MAMs alone (i.e. of MAMs on glass only) are also shown in the inset of the Figure 3.4(d). As can be seen from the figure, all OLEDs have very similar transmittance spectra, revealing that overall device transmittance does not change appreciably with M_{in}. This behavior is different from that observed in MAMs alone (i.e. in MAMs not integrated with devices) and indicates that maintaining geometrical symmetry in MAMs, and perhaps in all dielectric/metal/dielectric stacks in general, is not necessary for maximizing surface plasmon resonance or transmittance when these stacks are integrated with OLEDs. This may be attributed to the fact that, in an OLED, the organic layers underneath the MAM act as additional dielectric layers of somewhat similar refractive index, (e.g. the refractive indices of MoO_3 and Alq_3 at 600nm are ~1.71 and ~1.69, respectively [106 , 107]) and can, therefore, compensate for reductions in M_{in} thickness (i.e. when M_{in} is thinner than M_{out}).

It can also be seen from the spectra in 3.4(d) that the transmittance of the integrated device exceeds 45% over the 400-700 nm range, and is ~ 90% in the 450-475 nm range for all devices. Clearly, the electroluminescence peak of the devices (shown in the inset of Figure 3.4(c)) does not coincide with their transmittance peak. As noted above, the large difference between top and bottom luminance observed in all devices can be attributed to the fact that transmittance in the 520-570nm wavelength range, where the electroluminescence most strongly, is ~60-75%; lower than the peak transmittance. The relatively lower transmittance in this range may be the result of relatively higher MAM reflectivity at these wavelengths, resulting in an increase the ratio of the bottom to top luminance.

The above experimental results show that the 5nm inner MoO_3 layer plays an important role in improving the performance of the transparent OLEDs and the device with 5nm M_{in} exhibits the best performance in terms of turn-on voltage, brightness and transmittance. Nevertheless, the overall optical transmittance of the transparent OLED is still rather limiting, particularly over the wavelength range beyond 550 nm (transmittance below 70%). Figure 3.5 shows the transmittance spectra of three different structures: (i) a MAM alone (on glass), (ii) the same OLED configuration without the MAM cathode (i.e. only the organic layers + ITO + glass), and (iii) a full OLED including the MAM cathode. It shows that the organic layers + ITO +glass combination is quite transparent over the wavelength range of 450-700 nm (transmittance ~90-100%). The transmittance of the MAM shows a slow decrease in transmittance (90% to 63%) as the wavelength goes from 450 nm to 700 nm. On the other hand, the full OLED shows a narrower transmittance peak in the 400-500 nm, and faster decrease in transmittance in the 450-550 nm, resulting in a lower transmittance in the 450-700 nm range. At the OLED peak emission wavelength (522 nm), the transmittance of the device is only ~ 75%. Comprehensive optical modeling of a multiple layer structure consisting of the organic materials and MAM multilayer is needed to fully understand the degraded transmittance and to further optimize the device performance of this transparent OLED.

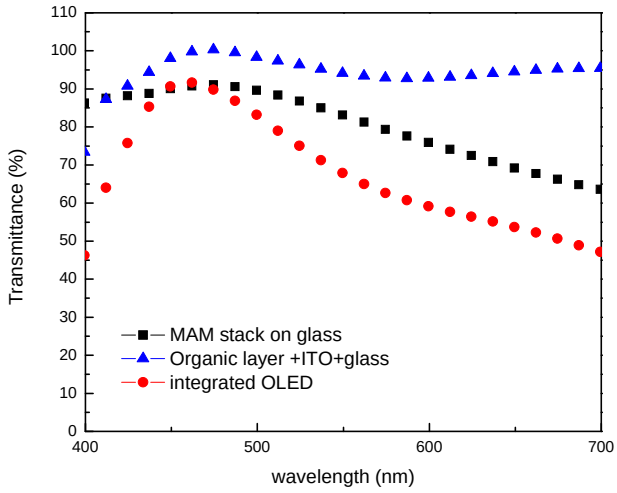

Figure 3.5: The optical transmittance of the different layer structures: a MoO_3/Ag/MoO_3 multilayer (square symbol), the organic layers in the transparent OLEDs (triangle symbol), and the combination of the former two (circular symbol).

3.1.3 Optimized transparent OLEDs with MAM cathode

As mentioned above, all transparent OLEDs have very similar transmittance spectra, revealing that overall device transmittance does not change appreciably with M_{in}. This behavior is different from that observed in MAMs alone (i.e. in MAMs not integrated with devices) and indicates that maintaining geometrical symmetry in MAMs, and perhaps in all dielectric /metal /dielectric stacks in general, is not necessary for maximizing surface plasmon resonance or transmittance when these stacks are integrated with OLEDs. This may be attributed to the fact that, in an OLED, the organic layers underneath the MAM act as additional dielectric layers of somewhat similar refractive index. And results suggest that device with 5nm M_{in} shows the best performance, it is reasonable to wonder if other two layers of Ag and Mout have to modify their thickness to optimize the device performance.

Accordingly, the MoO_3/Ag/MoO_3 structure was reconsidered in real transparent OLEDs. Since 5nm inner MoO_3 showed a promising performance, other series of OLEDs with 5nm inner MoO_3 and varied thicknesses of Ag as well as outer MoO_3 were fabricated and tested, shown in Figure 3.6 and 3.7, respectively.

(a)

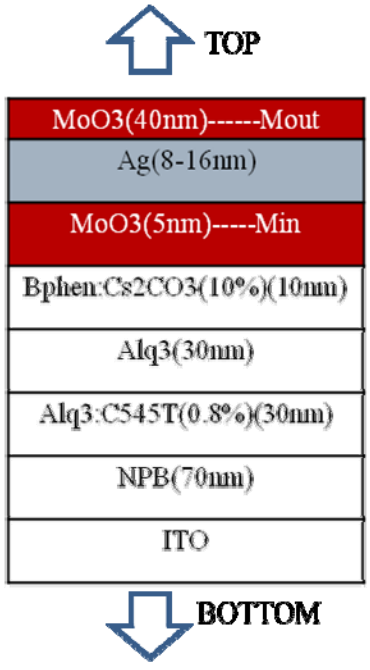

(b)

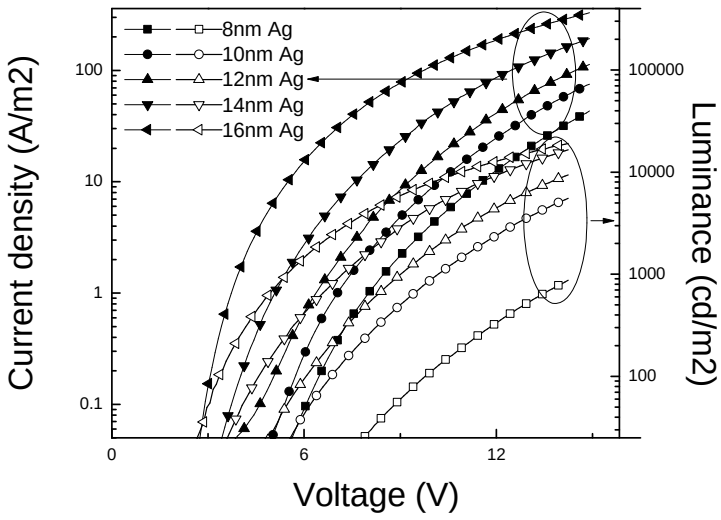

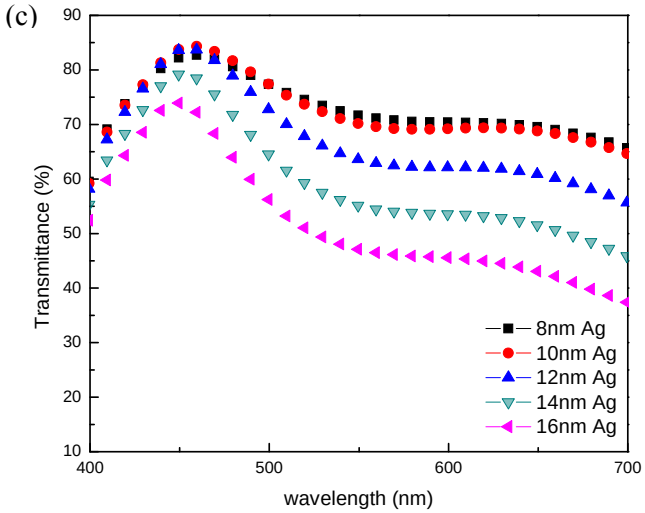

Figure 3.6: (a) Schematic layer structure of the transparent OLED with a MoO_3 M_{in} (5nm)/Ag (*x* nm)/ MoO_3 M_{out} (40nm) cathode. (b) The current density-voltage (J-V, solid symbols) and luminance-voltage (L-V, open symbols) characteristics (in Log scale) of the OLEDs with different inner Ag thicknesses. (c) The transmittance spectra through all device layers for the OLEDs with different Ag thickness.

Figure 3.6 (a) is schematic layer structure of the transparent OLED with a MoO_3 M_{in} (5nm)/Ag (*x* nm)/ MoO_3 M_{out} (40nm) cathode. Figure 3.6 (b) and (c) show the J-V-L characteristics and optical transmittance of devices with varied Ag thicknesses from 8nm to 16nm, respectively. As Ag thickness increases, the transmittance of the device decreases as shown in Figure 3.6 (c). It turns out that the device with 14nm Ag was superior to the devices with other Ag thicknesses under constant current density of 20mA/cm^2, bottom luminance of 1130 Cd/m^2 and top luminance of 263 Cd/m^2 (see Figure 3.6 (b)). The dependence of the device optical transmittance on the thickness of outer MoO_3 was stronger than that of Ag and M_{in}, seen in Figure 3.7. Figure 3.7 (a) is schematic layer structure of the transparent OLED with a MoO_3 M_{in} (5nm)/Ag (14 nm)/ MoO_3 M_{out} (*x* nm) cathode. Figure 3.7 (b) and (c) show the J-V-L characteristics and optical transmittance of devices with varied M_{out} thicknesses from 20nm to 200nm, respectively.

The M_{out} thickness is varying in a relative large region, so surface plasma resonance is very different in these devices. See in Figure 3.7(b), devices with 40nm and 80nm M_{out} show the best performance (i.e. luminance). However, devices with M_{out} thicker than 80nm have a much poor

transmittance. Therefore, the device with 40nm M_{out} has the best performance overall. To sum up, the MoO_3 (5nm)/Ag (14nm)/MoO_3 (40nm) structure used in this work had the best performance.

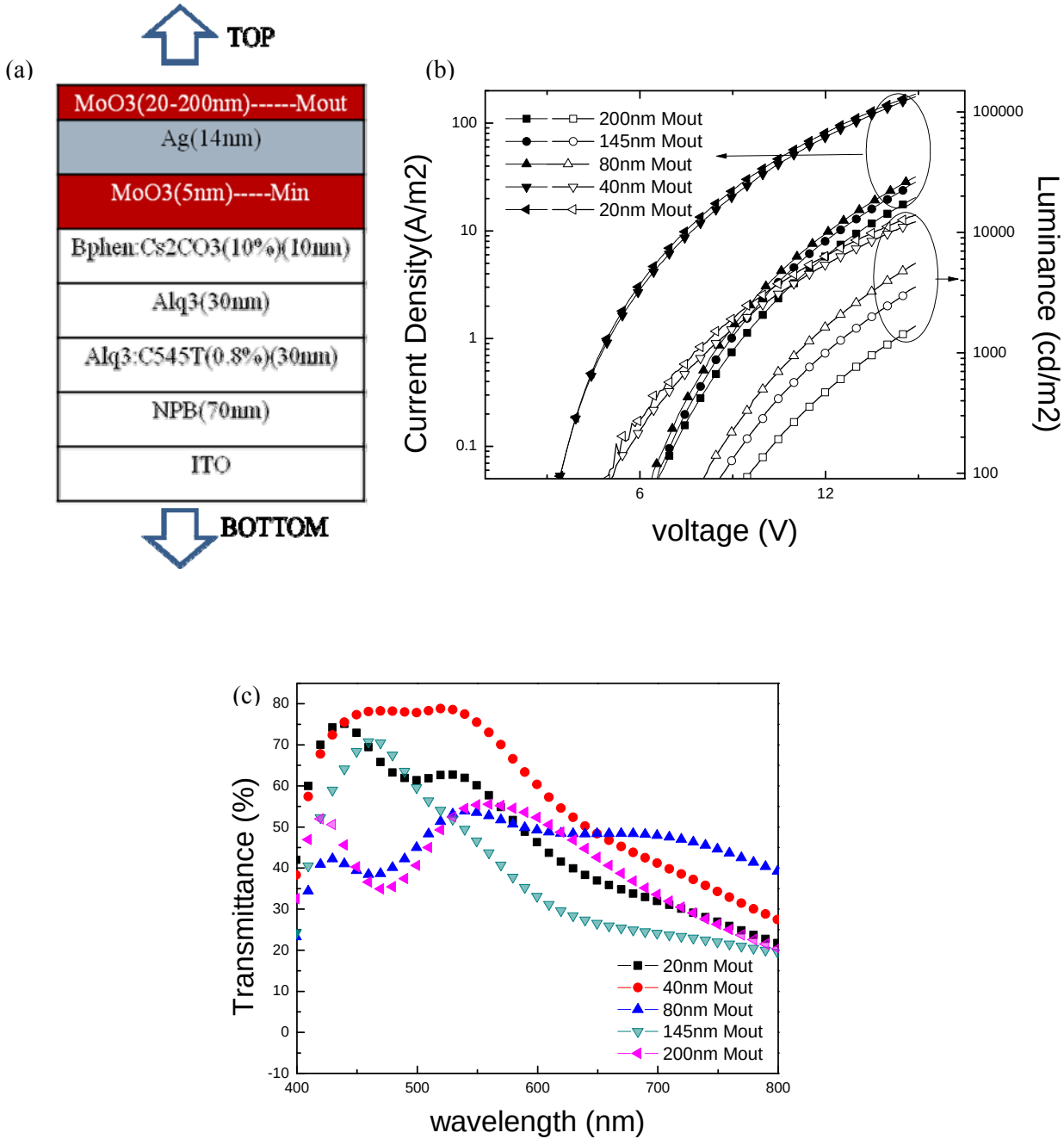

Figure 3.7: (a) Schematic layer structure of the transparent OLED with a MoO_3 M_{in} (5nm)/Ag (14 nm)/ MoO_3 M_{out} (*x* nm) cathode. (b) The current density-voltage (J-V, solid symbols) and luminance-voltage (L-V, open symbols) characteristics (in Log scale) of the

OLEDs with different inner M_{out} thicknesses. (c) The transmittance spectra through all device layers for the OLEDs with different M_{out} thickness.

In conclusion, MAM stacks are investigated for utilization as transparent cathodes in OLEDs. The stacks can be fabricated using simple thermal evaporation at relatively low temperatures, and can be readily and safely utilized as top electrodes, without causing deposition damage to the organic layers. Results show that it is possible to achieve efficient electron injection from the MAM electrode into organic layers by means of incorporating a suitable EIL at the cathode-organic interface. Results also show that a MAM stack can exhibit high optical transmittance, amounting to 65-80% in the 400-700nm, and a low sheet resistance (9Ω/□). A transparent OLED with a MAM cathode incorporated with a 10nm Bphen: Cs_2CO_3 (10%) EIL is studied. By fine tuning the MAM structure, optimal OLED performance is achieved: a total luminance of 1300 cd/m^2 (representing ~1000 cd/m^2 and ~300 cd/m^2 from the bottom and the top, respectively) at 20mA/cm^2 and a corresponding driving voltage of 7.2V. The OLED exhibits a peak transmittance of ~ 90% in the 450-475 nm range, and a transmittance above 45% over the entire visible (i.e. 400-700 nm) range.

3.2 Enhanced Bulk Conductivity and Bipolar Transport in Mixtures of MoO_3 and Organic Hole Transport Materials[†]

Since we introduce an EIL in our TOLEDs, the device performance is significantly improved. We attribute it to the improvement of the electron injection. However, the TOLEDs performance is still not superior. By improving the injection property and bulk conductivity of inner MoO_3 layer, we believe the device performance can be further improved. Introducing dopant in MoO_3 film is a logical train of thought to increase the conductivity of MoO_3 film, and dope MoO_3 with organic material could increase bulk conductivity comparing with neat MoO_3 which has been reported by Shin et al [97] and Ma et al [101]. However, these two groups showed different result of the conductivity increase in MoO_3 and HTM mixtures. In view of the tremendous growth and potential of the organic electronics industry, and the emergence of MoO_3 as an important enabling material, resolving this apparent discrepancy between the findings of the two studies becomes a matter of high scientific interest and technological importance.

[†] The main content of this section was submitted to Organic Electronics.

3.2.1 MoO_3 and NPB mixture in vertical structure

To resolving the discrepancy between the findings of the two studies by Shin et al [97] and Ma et al [101], a series of vertical structures of MoO_3 and NPB mixture, sandwiched by two electrodes, with different NPB concentration are fabricated and tested.

Figure 3.8 shows the I-V characteristics of 100nm thick films of neat MoO_3, neat NPB, and MoO_3:NPB (50%) mixture in vertical structures. Clearly, the current at any given voltage is higher in case of the MoO_3:NPB (50%) mixture than in case of the neat films.

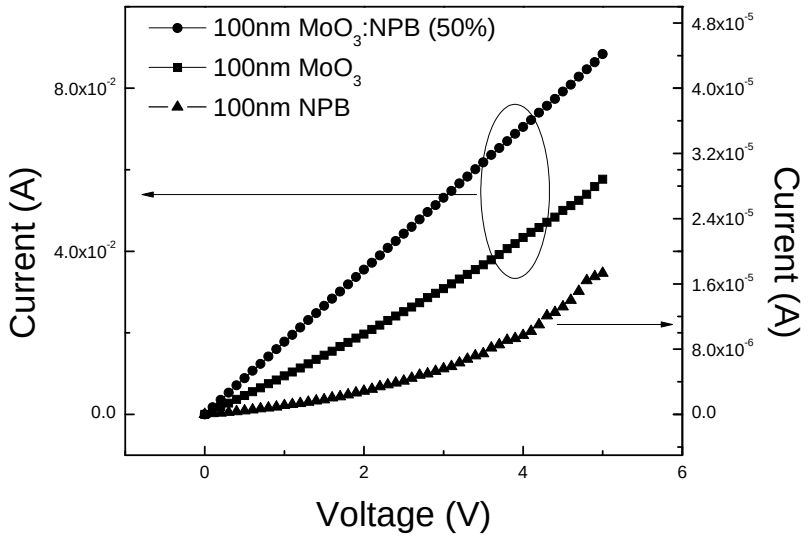

Figure 3.8: I-V characteristics of 100nm of MoO_3, NPB and MoO_3:NPB (50%) in a standard vertical structure

This is different from the results reported by both Shin et al [97] and Ma et al [101]. The discrepancy might be attributed to the use of vertical structures, which cause I-V characteristics highly sensitive to any small or subtle variations among test samples (e.g. small variations in ITO and/or film quality). The I-V characteristics of a thin film are typically affected by both material bulk conductivity and the carrier injection at the interface of the film/electrode. Since in a vertical structure the current flow path is across the film thickness (~100nm), the I-V behavior could be more strongly influenced by interfacial effects rather than by conduction across the film, causing bulk conductivity effects to be much less pronounced. To reduce this ambiguity, we use lateral structures that allow for a much longer current flow path (tens of micrometers) in the thin film material, thus make material bulk conductivity effects dominate the device I-V characteristics.

3.2.2 Enhanced Bulk Conductivity of MoO_3 and NPB mixture in lateral structure

Figure 3.9(a) shows I-V characteristics from a series of lateral devices with a 100 nm thick MoO_3:NPB layer of different MoO_3 concentrations, whereas Figure 3.9(b) displays the current at 10V in the devices versus MoO_3 concentrations. The inset of Figure 3.9(b) shows the schematic layer structure of these devices. In these devices, the current flow occurs from one Ag electrode to the other laterally across the 26 μm gap through the layer, under the applied bias. One can observe that all of the devices exhibit almost linear I-V characteristics over the voltage range of 0 – 20 V (see Figure 3.9(a)), while the current amplitude varies significantly from 10^{-11} to 10^{-5} A, depending on MoO_3 concentration. As the MoO_3 content increases from 0% (i.e. neat NPB) to 50% (MoO_3:NPB of 1:1), the current increases from 2×10^{-11} A to 1×10^{-5} A, corresponding to almost six orders of magnitude increase in conductivity. Interestingly, the current starts to decrease on further increasing MoO_3 content beyond 50% , and drops back to 2×10^{-10} A for x=100% (i.e. neat MoO_3). The data reveals that at the optimum composition, the MoO_3:NPB mixture demonstrates a conductivity that is almost five orders of magnitude higher than that of neat MoO_3.

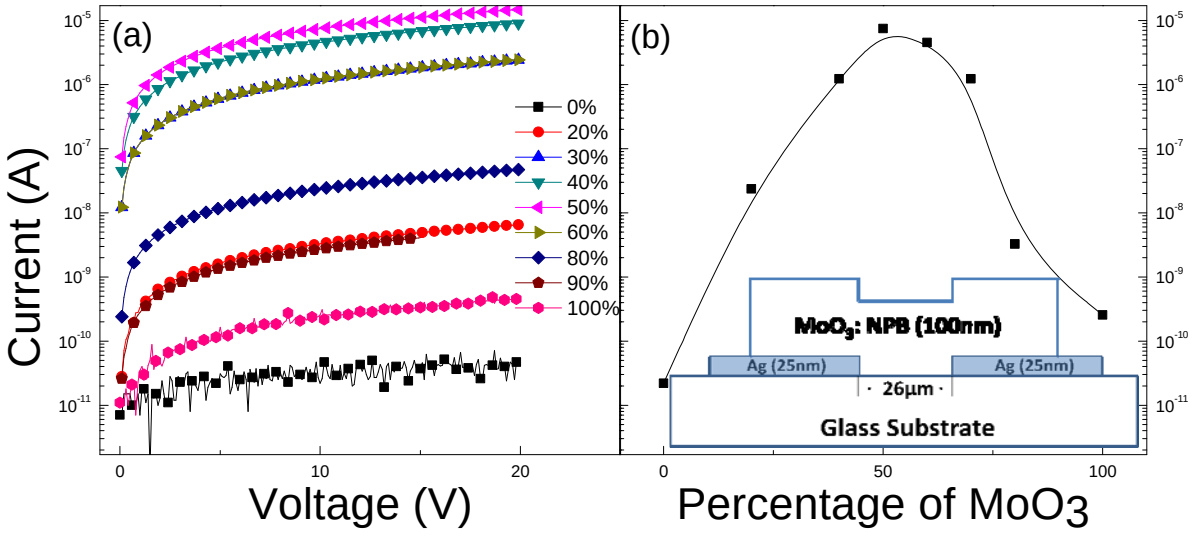

Figure 3.9: (a) The I-V characteristics of MoO_3:NPB(x %) films with 0 %< x % < 100 %. (b) The current of 100nm MoO_3:NPB(x %) films under 10V in lateral structure as a function of MoO_3 concentration (x %). The inset of Fig.3.9 (b) is the schematic layer structure of the lateral structure with 100nm NPB and MoO_3 mixture film.

The much higher conductivity demonstrated by the MoO_3:NPB mixture can be attributed to the formation of charge transfer complex between MoO_3 and the HTM [97], as was reported before from absorption spectra of such mixtures [97,108,109]. UV-Vis absorption measurements

on our films reveal the presence of a broad absorption band centered around 1400nm in case of the mixtures, consistent with those earlier reports. The charge transfer can be expected to increase "free" carrier density, and hence facilitate conduction in the mixture. It is therefore not surprising that the conductivity of the MoO_3:NPB mixture reaches its maximum at 50% MoO_3 content (i.e. at MoO_3:NPB ratio of 1:1) where optimal concentrations for maximal charge transfer complex formation may be expected.

While, in a lateral device, the changes in I-V with MoO_3 concentration can be expected to mostly arise from changes in bulk conductivity of the mixture layer, it is still possible that variations in charge injection at the metal contacts, associated with variations in MoO_3 concentration, affect the observations non-negligibly. Therefore, to investigate this possibility, we fabricate and test a series of lateral devices which all comprise a very thin (~10 nm thick) MoO_3 interfacial layer interposed between the metal contact and a thicker MoO_3:NPB mixture layer (~ 90 nm) of various MoO_3 content. The composition of the interfacial layer is kept the same in all devices. Figure 3.10 shows I-V characteristics of a series of lateral devices with a 10 nm MoO_3 interfacial layer and 90nm thick MoO_3:NPB layer of different MoO_3 concentrations. As can be seen from the figure, changing the MoO_3 concentration in the 90nm mixture layer changes the I-V characteristics in the same trend as before (i.e. Figure 3.9(a)) despite the presence of the interfacial layer in this case. Here again, a device with 50% MoO_3 content in the mixture layer gives the highest current. The results convincingly prove that the observed current enhancement in MoO_3:NPB mixture is primarily due to improvement in the bulk material conductivity.

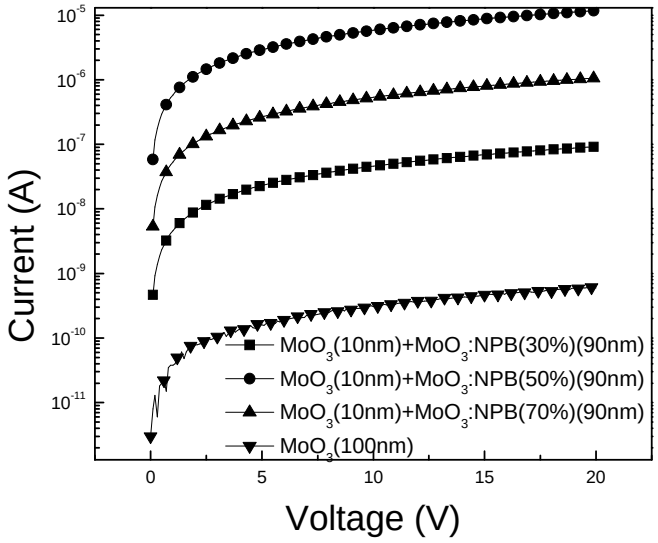

Figure 3.10: I-V characteristics of lateral devices with 100nm MoO_3, 10nm MoO_3 + 90nm MoO_3:NPB(30%), 10nm MoO_3 + 90nm MoO_3:NPB(50%), and 10nm MoO_3 + 90nm MoO_3:NPB(70%).

3.2.3 Mixtures of MoO_3 and different organic materials

To explore whether the observed conductivity improvement is unique to the MoO_3:NPB mixture, we test mixtures of MoO_3 with TCTA, as another HTM, and also mixtures of MoO_3 with tris(8-hydroxyquinoline) aluminum (Alq_3) or 4,7-diphenyl-1,10-phenanthroline (Bphen) as typical electron transport materials (ETMs). Figure 3.11(a) shows the I-V characteristics for lateral devices comprising a 100nm layer of MoO_3:TCTA (50%) mixture, and also for devices comprising a 100nm layer of neat TCTA or MoO_3 instead. Figure 3.11(b) shows the corresponding data set for the case of NPB for comparison. Clearly, similar to the case of MoO_3:NPB, a MoO_3:TCTA mixture demonstrates more than five orders of magnitude conductivity increase versus the neat TCTA or MoO_3 films. The results suggest that the bulk conductivity enhancement might be common to a wide range of MoO_3 and HTM mixtures. On the other hand, mixing MoO_3 with Alq_3 or Bphen does not show the same effect, as evident in Figure 3.11(c) and Figure 3.11(d), where in both cases, the current at any given voltage for the MoO_3:ETM mixture falls in-between that of the neat MoO_3 and ETM films, consistent with previous observations [101], indicating that the conductivity of the mixture does not surpass that of the neat materials.

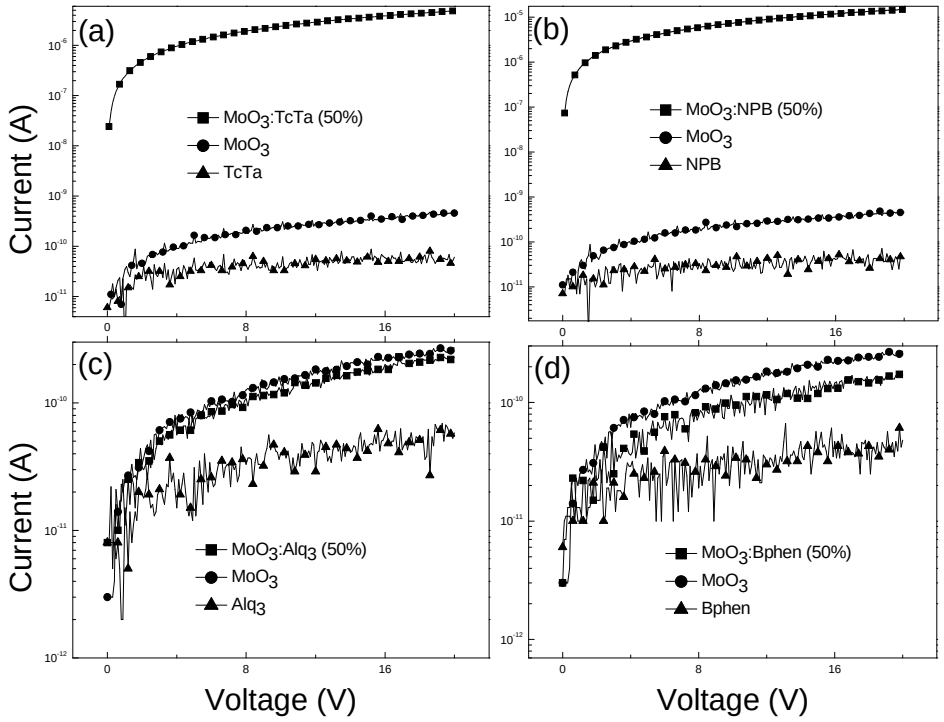

Figure 3.11: I-V characteristics of (a) 100nm of MoO_3, TCTA and MoO_3:TCTA(50%); (b) 100nm of MoO_3, NPB and MoO_3:NPB(50%); (c) 100nm of MoO_3, Alq_3 and MoO_3:Alq_3(50%); (d) 100nm of MoO_3, Bphen and MoO_3:Bphen(50%) in the lateral structure.

3.2.4 Bipolar Transport in Mixtures of MoO_3 and Organic Hole Transport Materials

Finding that the conductivity enhancement does not occur in MoO_3:ETM mixtures, suggesting that the phenomenon may be restricted to MoO_3:HTM mixtures, it naturally becomes interesting to determine if the higher conductivity arises from increased unipolar or bipolar carrier transport. To investigate this effect we compare MoO_3:NPB mixture layers against neat NPB and Alq_3 layers in "hole-only" and "electron-only" vertical device configurations. For this, we adopt the previously reported device architectures [110]: (i) ITO/ NPB (100nm)/ MoO_3:NPB (50%) mixture or neat NPB (100nm)/ NPB (100nm)/ NPB: 2,3,5,6-tetrafluoro-7,7,8,8-tetracyanoquinodimethane (F_4-TCNQ) (9:1) (10nm)/ Mg:Ag (9:1) (60nm); and (ii) ITO/ Mg (2nm)/ (Alq_3) (40nm)/ MoO_3:NPB (50%) mixture or neat Alq_3 (40nm) / Alq_3 (40nm)/ Mg:Ag (9:1) (60nm), for hole-only and electron-only devices, respectively. As, in these configurations, the layer of interest is sandwiched between either two hole transport layers or two electron transport layers, current flow will proceed primarily through the transport of either holes or electrons,

respectively. Figure 3.12(a) and 3.12(b) display I-V characteristics and schematic layer structure of these devices, respectively. As can be seen from the figure, the use of MoO_3:NPB mixture layer leads to a much higher current in both hole-only and electron-only devices in comparison to neat NPB or neat Alq_3, respectively. The results indicate that the MoO_3:HTM demonstrates enhanced transport of both holes and electrons, revealing it is bipolar in nature. This differs from the widely accepted view that introducing MoO_3 into an organic charge transport material generally suppresses electron transport due to its functionality as a p-type dopant [85-94]. Our results are supportive with recent findings by Kahn et al [111] that MoO_3 may also act as an n-type material. Our data suggests that the bulk conductivity enhancement in MoO_3:NPB mixtures may stem from its bipolar transport characteristics. Clearly, more work is needed to elucidate the mechanisms behind these extraordinary material properties.

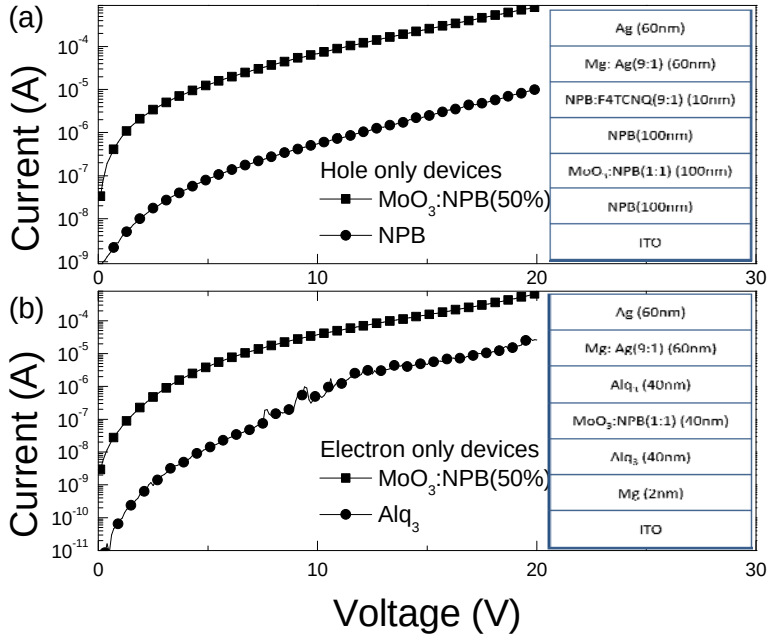

Figure 3.12: I-V characteristics of hole only and electron only devices: (a) hole only device with structure of ITO/ NPB (100nm) / NPB or MoO_3:NPB (50%) (100nm) / NPB (100nm) / NPB:F4TCNQ (10nm)/ Mg:Ag (9:1) / Ag, and (b) electron only device with structure of of ITO/ Mg (2nm) / Alq3 (40nm) / Alq3 or MoO_3:NPB (50%) (40nm) / Alq3 (40nm) / Mg:Ag (9:1) / Ag. The insets are the schematic layer structure of the hole only and electron only structure.

In conclusion, we systematically investigate the conductivity of thin films of mixtures of MoO_3 and hole transport materials (HTM) as a function of MoO_3 concentration. In order to better

resolve and differentiate between contributes form injection and bulk transport, the materials are studied in lateral devices in addition to the more conventional vertical device configuration. The results show that mixing MoO_3 with a hole transport material, such as NPB or TCTA brings about >5 orders of magnitude increase in bulk conductivity over that of neat MoO_3 or neat HTM. The results also show that the mixing enhances both hole and electron transport. The findings shed the light on the potential of hybrid composites of inorganic and organic materials in realizing enhanced conductivity.

Chapter 4

Conclusion

In conclusion, MAM stacks are investigated for utilization as transparent cathodes in OLEDs. The stacks can be fabricated using simple thermal evaporation at relatively low temperatures, and can be readily and safely utilized as top electrodes, without causing deposition damage to the organic layers. Results show that it is possible to achieve efficient electron injection from the MAM electrode into organic layers by means of incorporating a suitable EIL at the cathode-organic interface. Results also show that a MAM electrode can exhibit high optical transmittance, amounting to 65-80% in the 400-700nm, and a low sheet resistance (9Ω/□). A transparent OLED with a MAM cathode incorporated with a 10nm Bphen: Cs_2CO_3 (10%) EIL is studied. By fine tuning the MAM structure, optimal OLED performance is achieved: a total luminance of 1300 cd/m^2 (representing ~1000cd/m^2 and ~300cd/m^2 from the bottom and the top, respectively) at 20mA/cm^2 and a corresponding driving voltage of 7.2V. The OLED exhibits a peak transmittance of ~ 90% at a wavelength of 450-475 nm.

We also systematically investigate the conductivity of thin films of mixtures of MoO_3 and hole transport materials (HTM) as a function of MoO_3 concentration. In order to better resolve and differentiate between contributes form the injection and the bulk transport, the materials are studied in lateral devices in addition to the more conventional vertical device configuration. The results show that mixing MoO_3 with a hole transport material, such as NPB or TCTA brings about >5 orders of magnitude increase in bulk conductivity over that of neat MoO_3 or neat HTM. The results also show that the mixing enhances both hole and electron transport. The findings shed the light on the potential of hybrid composites of inorganic and organic materials in realizing enhanced conductivity.

Bibliography

[1] F. Garnier, R. Hajlaoui, A. Yassar & P. Srivastava, *Science* **265,** 1684(1994).

[2] Z. Bao, A. Dodalapur, A.J. Loving, Appl. Phys. Lett. **69**, 4108(1996)

[3] H. E. Katz, *J. Mater. Chem.* **7,** 369(1997).

[4] S. F. Nelson, Y. Y. Lin, D. J. GunYdlach & T. N. Jackson, *Appl. Phys.Lett.* **72,** 1854(1998).

[5] G. H. Gelinck, T. C. T. Geuns & D. M. de Leeuw, *Appl. Phys. Lett* **77,**1487(2000).

[6] V.C. Sundar, J. Zaumseil, V. Podzorov, E. Menard, R.L. Willett, T. Someya, M.E. Gershenson and J.A. Rogers, Science **303**, 1644 (2004)

[7] C. W. Tang & S. A. VanSlyke, *Appl. Phys. Lett.* **51,** 913(1987).

[8] J. H. Burroughes, D. D. C. Bradley, A. R. Brown, R. N. Marks, R. H. Friend, P. L. Burn & A. B. Holmes, *Nature (London)* **347,** 539(1990).

[9] R. H. Friend, R. W. Gymer, A. B. Holmes, J. H. Burroughes, R. N. Marks, C. Taliani, D. D. C. Bradley, D. A. dos Santos, J. L. Bre´das, M. Lo¨gdlund & W. R. Salaneck, *Nature (London)* **397,** 121(1999).

[10] U. Mitschke, P. Bauerle, J. Mater.Chem. **10**, 1471(200)

[11] D. Wohrle, D.Meissner, Adv. Mater. 3.129(1991)

[12] Sariciftci, N. S., Smilowitz, L., Heeger, A. J. & Wudl, F. (1992) *Science* **258,**1474–1476.

[13] Yu, G., Wang, J., McElvain, J. & Heeger, A. J. (1998) *Adv. Mater.* **17,** 1431–1434.

[14] Brabec, C. J., Sariciftci, N. S. & Hummelen, J. C. (2001) *Adv. Funct. Mater.* **11,**15–26.

[15] P.Peumans, A.Yakimov & S.R. Forrest, J.Appl.Phys. **93**, 3693(2003)

[16] J.G.Xue, S.Uchida, B.P. Rand & S.R. Forrest, Appl. Phys. Lett. **84**, 3013(2004)

[17] E.I.Iwuoha, M.R. Smyth & M.E.G. Lyons, Biosensors Bioelectron. **12**, 53(1997)

[18] J.S. Seo, D. Whang, H. Lee, S.I. Jun, J.Oh, Y.J. Jeon & K.Kim, Nature, **404**, 982(2000)

[19] T. Someya, Y. Kato, T. Sekitani, S. Iba, Y. Noguchi, Y. Murase, H. Kawaguchi & T. Sakurai, Proceedings of the National Academy of Sciences of the United States of America **102**, 12321(2005).

[20] M.A. Reed, J. Chen, A.M. Rawlett, D.W. Price, J.M. Tour, Appl.Phys.Lett, **78**, 3735(2001)

[21] L.P. Ma, J. Liu, Y. Yang, Appl.Phys.Lett, **80**, 2997(2002)

[22] S. Song, B. Cho, T.W. Kim, Y. Ji, M. Jo, G.Wang, M. Choe, Y.H. Kahng, H. Hwang, T.Lee, Adv. Mater. **22**, 5048(2010)

[23] T.N. Jackson, Y.Y. Lin, D.J. Gundlach, H. Klauk, IEEE J. Sel. Top.Quantum Electron. **4** (1998) 100.

[24] N. Suganuma, N. Shimoji, Y.Oku, S. Okuyama, K. Matsushige, Org.Electron. **9**, 834(2008)

[25] Hhttp://en.wikipedia.orgH.

[26] A. Bernanose, M. Comte, P. Vouaux, J. Chim. Phys. **50**, 64 (H1953H).

[27] M. Pope, H.P. Kallmann, and P. Magnante, J.Chem.Phys. **38**, 2042(1963)

[28] W. Helfrich, W.G. Schneide, Phys. Rev. Lett. **14**,229(1965)

[29] H. Shirakawa, E.J. Louis, A.G. Macdiarmid, G.K. Chiang, and A.J. Heeger, J.Chem.Soc.Chem.Comm. **16**, 578 (1977)

[30] P.S. Vincett, W.A. Barlow, R.A. Hann, and G.G. Robert, Thin Solid Films, **94**, 171(1982).

[31] G. Gustufsson, Y. Gao, G.M. Treacy, F. Klavetter, N. Colaneri, and A. Heeger, Naterue, **357**, 477(1992)

[32] Y. Gao, G.M. Treacy, P. Smith, and A. Heeger, Appl.Phys.Lett. **60**, 2711(1992)

[33] G. Gu, Z. Shen, P.E. Burrows, S.R. Forrest, Adv.Mater. **9**, 725(1997)

[34] M. Uchida, Y. Ohmori, C. Morishima, and K. Yoshino, Synth.Met. **57**, 4168(1992)

[35] G. Grem, G. Leditzky, B. Ulrich, G. Leising, Synth.Met. **51**,383(1992)

[36] I. Sokolik, Y. Zhou, F.E. Karasz, D.C. Morton, J.Appl.Phys. **74**, 3584(1993)

[37] P.L. Burn, A.B. Holmes, A. Kraft, D.D.C Bradley, A.R. Brown, R.H. Friend, and R.W. Gymer, Nature, **356**, 47(1992)

[38] Z. Yang, F.E. Karasz, and H.J. Geise, J.Polymer, **35**, 391(1994)

[39] M. Yan, L.J. Rothberg, F. Papadimitrakopoulos, M.E. Galvin, and T.M. Miller, Phys.Rev.Lett. **73**, 744(1994)

[40] J. Kido, K. Hongawa, K. Okuyama, K. Nagai, Appl.Phys.Lett. **64**, 815(1994)

[41] P. Dyreklev, M. Berggren, O. Inganas, M.R. Andersson, O. Wennerstrom, and T. Hjertberg. Adv.Mater, **7**, 43(1995)

[42] A.C. Fou, O. Onitsuka, M. Ferreira, M.F. Rubner, and B.R. Hsieh, J.Appl.Phys. **79**, 7501(1996)

[43] A.J. Epstein, J.W. Blatchford, Y.Z. Wang, S.W. Jessen, D.D. Gebler, L.B. Lin, T.L. Gustafson, H.L. Wang, Y.W. Park, T.M. Swager, and A.G. MacDiarmid, Synth.Met. **78**, 253(1996)

[44] T.R. Hebner, C.C. Wu, D. Marcy, M.H. Lu, J.C. Sturm, Appl.Phys.Lett. **72**, 519(1998)

[45] C.D. Muller, A. Falcou, N. Reckefuss, M. Rojahn, V. Wiederhirn, P. Rudati, H. Frohne, O. Nuyken, H. Becker, and K. Meerholz, Nature, **421**, 829(2003)

[46] www.universaldisplya.com

[47] www.cdt.co.uk

[48] I.D. Parker, J.Appl.Lett. **75**, 1656(1994)

[49] M.A. Lampert, P. Mark, Current Injection in Solids. New York: Academic Press Inc, 1970

[50] P.E. Burrows, Z. Shen, V. Bulovic, D.M. McCarty, S.R. Forrest, J.A. Cronin, M.E. Thompson, J.Appl.Lett. **79**, 7991(1996)

[51] S.R. Forrest, Nature **428**, 911(2004).

[52] SF.Chen, LL. Deng, J. Xie, et al. Adv.Mater. **22**(46), 5227(2010)

[53] G. Gu and S. R. Forrest, Appl. Phys. Lett. **68**,2606 (1996)

[54] M.-H. Lu, M. S. Weaver, T. X. Zhou, M. Rothman, R. C. Kwong, M. Hack, and J. J. Brown, Appl. Phys. Lett. **81**, 3921 (2002).

[55] H. Riel, S. Karg, T. Beierlein, B. Ruhstaller, and W. Riess, Appl. Phys. Lett. **82**, 466 (2003)

[56] V. Bulovic, P. Tian, P. E. Burrows, M. R. Gokhale, and S. R. Forrest, Appl.Phys. Lett. **70**, 2954 (1997).

[57] L. S. Hung and C. W. Tang, Appl. Phys. Lett. **74**, 3209 (1999).

[58] G. Parthasarathy, C. Shen, A. Kahn, and S. R. Forrest, J. Appl. Phys. **89**,4986 (2001).

[59] J.S. Huang, M. Pfeiffer, A. Werner, J. Blochwitz, S. Liu, and K. Leo, Appl.Phys. Lett. **80**, 139 (2002).

[60] D.H. Kim, D.W. Kim, M.P. Hong, Jpn.J.Appl.Phys. **47**,075672 (2008).

[61] G. Gu, V. Bulovic, P.E. Burrows, S.R. Forrest, M.E. Thompson, Appl. Phys. Lett. **68**, 2606 (1996).

[62] G. Parthasarathy, P.E. Burrows, V. Khalfin, V.G. Kozlov, S.R. Forrest, Appl. Phys. Lett. **72**, 2138 (1998).

[63] G. Parthasarathy, C. Adachi, P.E. Burrows, S.R. Forrest, Appl. Phys. Lett.**76**, 2128 (2000).

[64] P.E. Burrows, G. Gu, S.R. Forrest, E.P. Vicenzi, T.X. Zhou, J. Appl. Phys.**87**, 3080 (2000).

[65] H. Murakami, M. Shimizu, S. Aratani and M Tanaka, Jpn. J. Appl. Phys. **48**.8 (2009)

[66] T. Dobbertin, M. Kroeger, D. Meithecker, D. Schneider, D. Metzdouf, H.Neuner, E. Becker, H.-H. Johannes, W. Kowalsky, Appl. Phys. Lett. **82**, 284 (2003).

[67] C.H. Jeong, J.T. Lim, J.H. Lee, M.S. Kim, J.W. Bae, G.Y. Yeom, Jpn. J. Appl. Phys., Part 1 Regul. Pap. Brief Commun. Rev. Pap. **45**(10B), 8457 (2006).

[68] S. Y. Ryu and H. K. Baik, Appl. Phys. Lett. **90**, 033513 (2007).

[69] J.C.C. Fan, F.J. Bachner, H. Foley, P.M. Zavracky, Appl.Phys.Lett. **25**, 693 (1974)

[70] M. bender, W. Seelig, C. Daube, H. Frankenberger, B. Ocker, and J. Stollenwerk, Thin Solid Films, **326**, 67 (1998).

[71] M. Fahland, P. Karlsson, and C. Charton, Thin Solid Films, **392**, 334 (2001).

[72] Y.S. Park, H.K. Park, J.A. Jeong, H.K. Kim, K.H. Choi, S.I. Na, and D.Y. Kim, J. Electrochem. Soc. **156**, H588 (2009).

[73] J. Lewis, S. Grego, B. Chalamala, E. Vick, D. Temple, Appl. Phys. Lett. **76**, 259, (2004).

[74] S.Y. Ryu, J.H. Noh, B.H. Hwang, C.S. Kim, S.J. Jo, J.T. Kim, H.S. Jeong, C.H. Lee, S.Y. Song, S.H. Choi, S.Y. Park, Appl. Phys. Lett.**92**, 023306, (2008).

[75] H.Q. Pang, Y.B. Yuan, Y.F. Zhou, J.R. Lian, L.F. Cao, J. Zhang, X. Zhou, J. of Luminescence **122**,587 (2007).

[76] X.J. Liu, X. Cai, J.S. Qiao, H.F. Mao, N. Jiang, Thin Sol. Films **441** ,200 (2003).

[77] C. Tao, G. Xie, C. Liu, X. Zhang, W. Dong, F. Meng, X. Kong, L. Shen, S. Ruan, and W. Chen, Appl. Phys. Lett. **95**, 053303 (2009).

[78] S. Tokito, K. Noda, and Y. Taga, J. Phys. D. **29**(11), 2750 (1996).

[79] H. Kanno, R. J. Holmes, Y. Sun, S. Kena-Cohen, and S. R. Forrest, Adv. Mater. (Weinheim, Ger.) **18**, 339 (2006).

[80] C. W. Chen, Y. J. Lu, C. C. Wu, E. H. Wu, C. W. Chu, and Y. Yang, Appl. Phys. Lett. **87**, 241121 (2005).

[81] T. Matsushima, Y. Kinoshita, and H. Murata, Appl. Phys. Lett. **91**, 253504 (2007).

[82] H. Lee, S. W. Cho, K. Han, P. E. Jeon, C.-N. Whang, K. Jeong, K. Cho, and Y. Yi, Appl. Phys. Lett. **93**, 043308 (2008).

[83] T. Matsushima, G.-H. Jin, and H. Murata, J. Appl. Phys. **104**, 054501(2008).

[84] N. Tokmoldin, N. Griffiths, D. D. C. Bradley, and S. A. Haque, Adv.Mater. (Weinheim, Ger.) **21**, 3475 (2009).

[85] S. Tokito, K. Noda, and Y. Taga, J. Phys. D **29**, 2750 (1996).

[86] K. J. Reynolds, J. A. Barker, N. C. Greenham, R. H. Friend, and G. L.Frey, J. Appl. Phys. **92**, 7556 (2002).

[87] T. Matsushima, Y. Kinoshita, and H. Murata, Appl. Phys. Lett. **91**, 253504 (2007).

[88] H. J. Bolink, E. Coronado, J. Orozco, and M. Sessolo, Adv. Mater. (Weinheim,Ger.) **21**, 79 (2009).

[89] K. Kanai, K. Koizumi, S. Ouchi, Y. Tsukamoto, K. Sakanoue, Y. Ouchi, and K. Seki, Org. Electron. **11**, 188 (2010).

[90] C. Wu, C. T. Lin, G. R. Lee, T. Y. Cho, C. C. Wu, and T. W. Pi, J. Appl.Phys. **105**, 033717 (2009).

[91] S. Hamwi, J. Meyer, T. Winkler, T. Riedl, and W. Kowalsky, Appl. Phys.Lett. **94**, 253307 (2009).

[92] M. Kröger, S. Hamwi, J. Meyer, T. Riedl, W. Kowalsky, and A. Kahn,Appl. Phys. Lett. **95**, 123301 (2009).

[93] G. H. Xie, Y. L. Meng, F. M. Wu, C. Tao, D. D. Zhang, M. J. Liu, Q. Xue, W. Chen, and Y. Zhao, Appl. Phys. Lett. **92**, 093305 (2008).

[94] T. Matsushima and C. Adachi, J. Appl. Phys. **103**, 034501 (2008).

[95] X. Zhu, J. Sun, X. Yu, M. Wong, H.S. Kwok, Jpn. J. Appl. Phys. **46**, 1033 (2007).

[96] J.H. Li, J. Huang, Y. Yang, Appl. Phys. Lett. **90**, 173505 (2007).

[97] W.-J. Shin, J.-Y. Lee, J. C. Kim, T.-H. Yoon, T.-S. Kim, and O.-K. Song,Org. Electron. **9**, 333 (2008).

[98] V. Shrotriya, G. Li, Y. Yao, C. Chu, Y. Yang, Appl. Phys. Lett. **88**, 073508 (2006).

[99] A.K.K.Kyaw, X.W.Sun, C.Y.Jiang, G.Q.Lo, D.W.Zhao, and D.L.Kwong, Appl. Phys. Lett.**93,** 221107 (2008).

[100] H. Ikeda, J. Sakata, M. Hayakawa, T. Aoyama, T. Kawakami, K. Kamata,Y. Iwaki, S. Seo, Y. Noda, R. Nomura, and S. Yamazaki, SID Int. Symp.Digest Tech. Papers **P-185**, 923 (2006).

[101] X.F. Qiao, J.S. Chen, X.L. Li, D.G. Ma, J. Appl.Phys. **107**, 104505 (2010)

[102] J. Kido, T. Matsumoto, Appl. Phys. Lett. **73**, 2866 (1998).

[103] H.J. Ding, K. Park, Y.L. Gao, J. Electron Spectrosc. Relat. Phenom. **174**, 45 (2009).

[104] F. Li, H. Tang, J. Anderegg, and J. Shinar, Appl. Phys. Lett. **70**, 1233 (1997).

[105] Z. B. Deng, X. M. Ding, S. T. Lee, and W. A. Gambling, Appl. Phys. Lett. **74**, 2227 (1999).

[106] R. Cardenas, J. Torres, and JE. Alfonso, Thin Solid Films. **478**, 146(2005).

[107] P. Dalasinski, Z. Lukasiak, M. Rebarz, M. Wojdyla, A. Bratkowski, and W. Bala, Opto-Electronics Review, **12**, 04429(2004)

[108] C. Ganzorig, M. Fujihira, Appl. Phys. Lett. **77**, 4211 (2000).

[109] J. Endo, T. Matsumoto, J. Kido, Jpn. J. Appl. Phys. **41**,358 (2002).

[110] Y. C. Luo, H. Aziz, Z. D. Popovic, and G. Xu, Chem. Mater. **19**, 2288 (2007).

[111] J. Meyer, A. Shu, M. Kroger, and A. Kahn, Appl.Phys.Lett. **96**, 133308 (2010)